

Airborne geomagnetic mapping with an unmanned aerial vehicle: development of a sensor calibration scheme

Master Thesis

Submitted by:

Aubert Franco

faubert@student.ethz.ch

Under the supervision of:

Dr. Friedemann Samrock, ETH, Institute of Geophysics, Zürich

Co-referee:

Prof. Dr. Evert Slob, TU, Faculty of Civil Engineering and Geosciences, Delft

Prof. Dr. Alexey Kuvshinov, ETH, Institute of Geophysics, Zürich

Zürich, 5th August 2022

1. Table of Content

1. Table of Content.....	2
2. Abstract.....	4
3. Introduction.....	5
4. Equipment and procedure.....	7
4.1 UAV.....	7
4.2 Mission planner.....	8
4.3 Sensors and processing software.....	10
4.4 Datasets.....	12
4.5 Processing steps.....	13
5. Sources of unwanted magnetic influences and other inaccuracies.....	16
5.1 Azimuthal error.....	16
5.2 Tilting error.....	17
5.3 Positioning related errors.....	18
5.4 Dual sensor differences.....	21
5.5 Color coding of data.....	23
5.6 Case in point from Forel.....	24
6. Development of correction techniques.....	28
6.1 Survey design.....	28
6.2 Heading error solution.....	30
6.2.1 Distant sensor solution.....	30
6.2.2 Scalar calibration and compensation for magnetization.....	31
6.2.3 Algorithm development.....	34
6.2.4 Example with latest Forel data.....	36
6.2.5 Gradient interpretation.....	39
6.3 Topography positioning corrections.....	43
6.4 Color coding for qualitative interpretation.....	45

7. Conclusion.....	49
8. References.....	50
9. Appendix.....	52
9.1 Survey Matlab script to find parameters for the scalar calibration of one sensor.....	52
9.2 Matlab function to calculate the misfit.....	58
9.3 Matlab function to generate the matrices and the vector.....	59
9.4 Forel orthophoto (June 2022).....	60
9.5 Forel magnetic map (June 2022).....	61
9.6 Forel gradient map (June 2022).....	62
9.7 Declaration of originality.....	63
10. Funding and acknowledgements.....	64

2. Abstract

In the last decade, technological advances in the field of multicopters enabled a widespread use of drones that include professional research applications covering a wide field from civil engineering to geosciences and agriculture. In recreational spheres drones became popular for sport and leisure activities like private photography. In geophysics, multicopters opened new doors for easier and cheaper airborne surveying especially with electromagnetic sensors such as geomagnetometers and georadar.

In this study we developed an airborne geomagnetic mapping system by combining commercially available components. Our setup consists of a DJI M600 drone with a SENSYS Magdrone R3 sensor mounted on the drone's landing gear. First measurements showed that data processing requires correcting for the multicopter's varying orientation during the flight, which impacts the magnetic recordings. The correction of this so-called heading error can be addressed using a scalar calibration scheme, which was originally developed for satellite missions. The calibration is performed by a specific maneuver in flight and compensates the vehicles magnetic influence on the magnetic recordings. We demonstrate how a high data quality can be achieved using a newly developed calibration algorithm for our drone-sensor-setup and how geomagnetic data can be processed in such a way that a reliable qualitative interpretation is achievable.

In a case study we conducted an airborne geomagnetic mission in Forel (FR, Switzerland) at a military bombing range near Payerne, which is used as a training facility for target practices. The study area consists of an inaccessible swamp and shallow water zone, where ammunition was documented to be shot and dumped throughout the last century. The results show that our setup allows to reliably locate magnetic anomalies as they are produced by dropped ammunition. Therefore, fast and safe geomagnetic surveying is possible, and it can aid in future not only for UXO detection but also for identifying abandoned landfills and geological structures.

3. Introduction

Geomagnetism is a branch of geophysics which focuses on the study of the Earth's magnetic field and its fluctuations over time and space. The geomagnetic measurements describe the sum of all fields, coming from different magnetic sources which range from the convection of the Earth's iron core to the solar wind impacting the ionosphere. These geomagnetic observations require highly sensitive and precise sensors called geomagnetometers or magnetometers in order to observe weak signal changes.

Magnetometers are devices that record magnetic fields in a 3-axis vectorial or scalar form. They can be composed of different parts that rely on different physical principles to carry out the measurements. Among the most known magnetometers there are fluxgate-type, proton-precession, cesium vapor etc.

The magnetometers are either placed at a fixed location, to observe temporal variations, in places such as the observatories in Chambon la Forêt, France or at Lanzhou, China (Geomagnetic observatories catalog, 2022), or are carried over an area of interest to observe spatial variations. In both cases, it is the variations of the magnetic field that carry information about the nature of the source, i.e. the relative amplitude difference of the so-called anomaly and the mean.

The applications of spatial variation surveys range from unexploded ordnance (UXO)-detection, to archeological investigation, geological structure identification etc. (Nabighan et al., 2005). Such objects and structures can be revealed provided that there is a lateral magnetic contrast. The presence of UXO for example requires high resolution data in order to identify smaller objects. A qualitative interpretation of the data can be done after performing signal analysis which includes compensating for temporal variations and electrical apparatus interferences. Quantitative interpretation is always much more difficult because of the ambiguity problem. This problem is that identical anomalies in the data can be generated by different objects, at different depths with different magnetizations.

Numerous forms of surveying exist in the case of geomagnetic spatial investigations, for instance, man-carried or vehicle towed surveys (land, sea, air). All forms of surveying that have the sensor close to metallic/magnetic bodies or vehicles require a calibration of the measurements to account for the introduced error. This correction is not necessary if the survey is designed in such way that the device is always held in the identical orientation and identical tilting with respect to the carrier and moving in a constant azimuth because the error is a constant throughout the whole survey.

The data in this research will consist of airborne (spatial) geomagnetic measurements and stationary measurements. We will be using an unmanned aerial vehicle (UAV or drone) with a geomagnetometer attached to its landing gear, held unretracted for this purpose. The results observed in previous research by Aubert (2019) showed that the magnetic data acquired by drone required a correction for the sensor's orientation and inclination, also called heading error. The stationary measurements were

performed simultaneously by a base station located not far from the airborne survey. The corresponding dataset was used to correct the airborne dataset for temporal variations.

First, the aim of this report is to assess the induced and permanent magnetization of the UAV itself on the measurements in 360° degree horizontal orientation and up to 25° vertical orientation and then develop an algorithm to automatically account for this error in the data during processing. This research will also focus on other possible sources of errors and inaccuracies and assess their influence on the measurements.

These other sources of influence include GPS-related positioning, the digital model terrain used for the automated missions and the dual sensor reciprocity for lateral consistency among others. Finally, the choice of color scale to visualize the data will be discussed in the final part of this research because it has an influence on how we present and see the results (Cramer et al. 2020).

The development of the calibration algorithm will be based on data that were acquired on field in Switzerland, Mongolia and Iceland in the past three years. The final calibration scheme will be applied to a real case study in collaboration with armasuisse, the federal office for defense procurement of Switzerland. Armasuisse is owner and responsible for the management of most military training areas and buildings in Switzerland.

The site of investigation for the final case study is located in Forel (Fribourg) Switzerland at the shore of the Lake Neuchâtel. It is used by the Swiss air force as a military bombing range since the last hundred years. This location was also used as a disposal area for old ammunition. However, the documentation does not state clearly the quantities and the type of ammunition that were dumped nor the exact location of such waste.

To conclude, this research will show that airborne geomagnetic measurements can be carried out in an effective way over a terrain where a man-carried survey is impossible and even dangerous and where boats cannot navigate. It will also demonstrate that processing with the further developed algorithm for heading error yields more consistent and more precise anomaly maps than without.

4. Equipment and procedure

Chapter 4 concentrates on the description of the materials used for the research, which include the UAV, the sensors, the softwares exploited to acquire and analyze the data and the datasets.

4.1 UAV

The UAV used for the surveys by Aubert (2019) during the past three years remains the same for this research. It is the DJI MATRICE 600 Pro, a hexacopter¹ with triple redundant flight controller (FC) modules called DJI A3. The UAV is also equipped with triple GPS antennas on top of the frame (one per FC) for more accuracy and redundancy in case of failure of one or two of the FCs (cf. Fig.1).

Main properties of the M600	
Payload capacity	6.0kg
Flying weight	9.5kg
Max takeoff weight	15.5kg
Flying time	15-30min (loaded-unloaded)
Max separation pilot-UAV	5.0km
Max flying altitude	500m relative to takeoff alt.
Max flying speed	18m/s

Table 1: Summary of the main properties of the UAV used in this research.

The M600 can be flown manually by the pilot or automatically using a pre-defined track with waypoints. In the case of geomagnetic surveys, one key to avoid complex topographic corrections is to fly at the same height above the ground throughout the entire survey. This can't be achieved manually but only with automated flights. These automated flights consist of a series of waypoints along the desired survey path. The UAV interpolates between them and follows the route as close as possible thanks to its GPS. Automated flights for UAVs are allowed per Swiss regulations (FOCA, 2022) as long as the pilot maintains visual contact with the aircraft during the entire flight.

The missions that are planned for the M600 always have to take into account the maximum flight time of the aircraft which is dependent on the load. In our case, the load comprises the geomagnetometer and a camera (thermal or visual) and is about 1.6kg in total. The speed of flying influences the overall duration of the mission but will reduce the spatial sampling if chosen too high and tends to introduce position-inaccuracies for the reason that latency appears due to the momentum of the UAV, in other words, the UAV doesn't have enough time to correctly adjust its flight path to the actual programmed track. The datasets were acquired with flying speeds between 7-11m/s (cf. 4.4 Datasets). Safe mission

¹ hexacopter stands for multirotor UAVs with 6 motors

durations were identified not to exceed 20min to avoid over-draining the batteries and to have a safety margin.



Fig.1: Photo of the M600, with its 6 propelled arms and 3 visible GPS antennas on top of the frame, equipped for a survey mission with the thermal camera and the geomagnetometer (attached to the landing skid).

4.2 Mission planner

One limiting factor with regard to the automated missions appears in the embedded software of the M600. In fact, the UAV cannot perform missions beyond the 99th waypoint, therefore survey missions need to be planned taking this into account. For very rough relief many waypoints ($\gg 99$) are required for accurate terrain following, it could be a solution to perform multiple smaller missions. In the case study later on, we will be flying over a swamp zone from a lake, mostly at constant altitude so this will not be a major issue.

The mission planner used to create the flight path over the survey area is called UgCS² from SPH Engineering, based in Latvia. This software allows for rapid mission planning of come-and-go type only requiring a manual input of edge points to delimit a survey area as shown by the red circles in Fig.2 A. The software then automatically generates a flight path with waypoints inside the given polygon conforming to the specified flight altitude, orientation relative to North and flying speed parameterized. The flight path, also called mission, can then be uploaded to the UAV's internal memory and executed from the take off point or directly in the air. It is also important to indicate what

² UgCS Universal ground Control Software

actions the UAV should undertake if the link with the operator is compromised. Among the possibilities there are “return home” and “continue mission”.

Furthermore, the operator can build multiple missions over larger areas and visualize these simultaneously in 3D to make sure that the entire area of interest is covered. As Fig.2 B shows, the missions have a small overlap in all directions. This overlap was purposely programmed and serves as reference for calibration of the measurements in order to get consistent scaling of the data and thus anomalies among the missions on the final map.

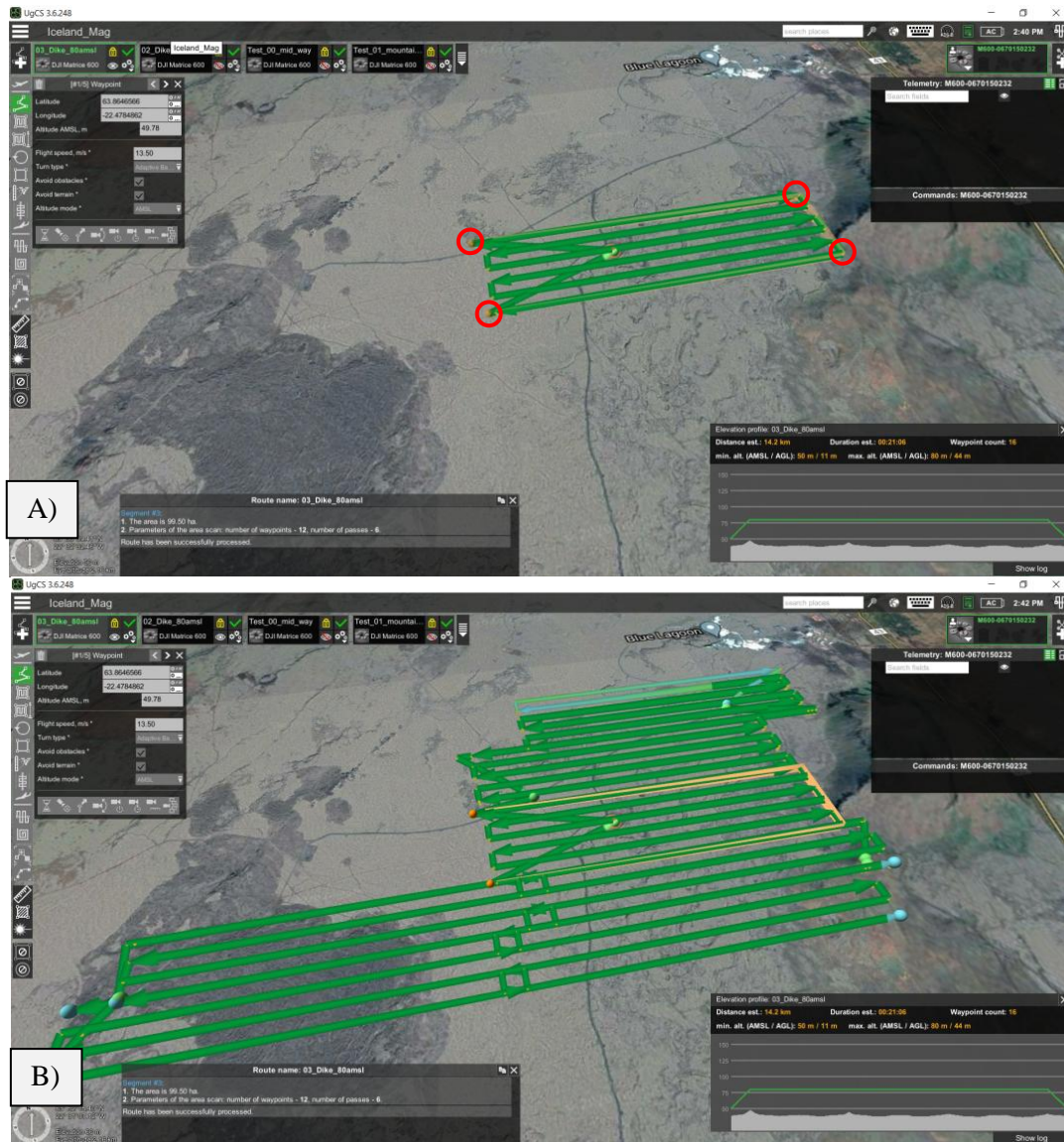


Fig.2: Screenshots of the mission planner UgCS; A) single mission planned using four edge points (red circles) and defining the altitude, flying speed and orientation, in total 16 waypoints were generated for this constant altitude mission. B) same mission as A) (in orange) with all the other missions from the project Iceland (cf. 4.4 Datasets).

4.3 Sensors and processing software

Various types of sensors exist for geomagnetic measurements. Proton precession magnetometers and optically pumped magnetometers (cesium-vapor e.g.) commonly serve in geomagnetic surveys due to their nearly absolute scalar measurements with an accuracy of up to 0.01nT (e.g. Munsch et al., 2007). Being less accurate and sensitive to detect very weak anomalies, fluxgate-type magnetometers record the components of the total field in a certain direction; this is why 3 orthogonal fluxgates sensors are needed to recover the absolute value.

The sensors used in this research are fluxgate-type geomagnetometers for the reason that they are generally much cheaper, lighter, more robust, have higher sampling rates and lower power consumption (e.g. Mathé et al., 2009). However, we will see later that calibration errors are a main weakness from these devices.

The airborne fluxgate magnetometer used is the MagDrone R3 from Sensys, a German based company. The base station is the MagBase also from Sensys. Both devices have identical sampling rate, measurement range and resolution. Table 2 indicates that there are actually two 3-axial fluxgates sensors in the MagDrone R3 separated by 1m; we will henceforth also refer to both datasets as two traces.

Sensys MagDrone R3	
N° of 3-axial sensors	2
Sensor separation	1.0m
Sensor type	Fluxgate
Autonomy (battery)	~3h (11.1V 1950mAh)
Sampling rate	200Hz
Measurement range	$\pm 75'000\text{nT}$
Resolution	$<0.3\text{nT}$
Weight	880g (without battery)

Table 2: Summary of the main properties of the geomagnetometer MagDrone R3 used in this research.

The B-field measured by the MagDrone R3 is recorded in its vectorial form, available as 3 datasets (x,y,z) per sensor. As mentioned in the introduction, the airborne survey dataset requires a temporal correction to remove the magnetic drift occurring during the time lapse of the mission. This correction requires a static measurement done by the base station. In the processing part, we will see that subtracting the static signal to the airborne signal yields a temporally corrected signal which doesn't contain the real total intensity anymore. Subtracting the mean results in a signal with only anomalies, which we are looking for.

The physical principle behind a fluxgate magnetometer relies on electromagnetism. Two thin copper-wires are rolled around a small ferromagnetic core and when changes in the ambient magnetic field occur, they change the core's permeability and thus its own B-field. These changes induce a voltage that is picked up by the red coil in Fig.3 B. If the current is run in the reverse direction through the copper-wire, the magnetic field direction also reverses (C). Rapid changes of current direction create an oscillating signal around 0 in the case of a magnetic-free environment. If an external magnetic field is applied then the signal no longer oscillates around 0 but around the value that corresponds to the ambient magnetic intensity (D). This device is called a fluxgate magnetometer. Finally, to be able to measure a magnetic field in 3 dimensions, at least 3 non-coplanar fluxgates are required and when the norm of their measurements is put together, we find a scalar vector containing the direction of the total field along with its intensity (Primdhal, 1979).

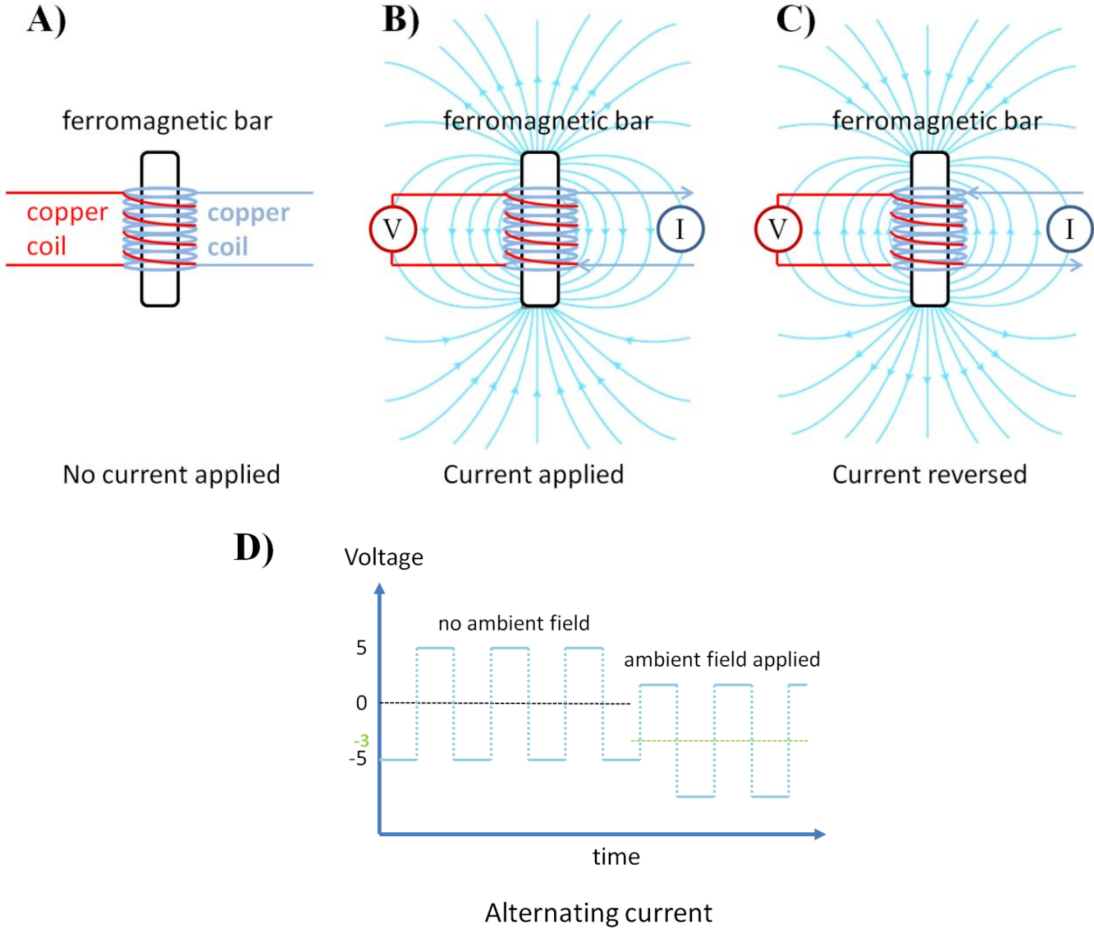


Fig.3: Sketches of the operating principle of a fluxgate geomagnetometer, consisting of A) a ferromagnetic bar rolled with two copper-wire coils; B) when a current is applied through one coil, a magnetic field is generated and a voltage is momentarily picked-up by the other coil; C) when the current is reversed, the magnetic field and voltage are also reversed. D) When the current is alternating, the values of the induced voltage oscillate around 0, and when an ambient magnetic field is applied to the sensor, the same oscillation appears shifted by an amount (here -3) representing the value of the ambient magnetic field.

According to Table 2, both the MagDrone and MagBase sensors have a sampling rate of 200Hz meaning that the spatial sampling density of the signal along the track is controlled by the flying speed. In the datasets used, the flying speed was typically between 7-11m/s, this corresponds to a measurement spacing ranging from 3.5-5.5cm. The software used to perform the processing is called Matlab³. Matlab is able to compute complex algorithmic calculations with a discrete signal at a relative cheap computational cost and also contains visualization tools to display the data on a 2D map which can then be placed above a satellite image using Google Earth Pro or GIS for example.

4.4 Datasets

The datasets used for this research come from three different survey projects. They were all conducted by the same personnel and with the same equipment described above over different places in the world. Table 3 summarizes the important information regarding these datasets.

Table of the dataset's locations					
Country	Location	Date	Magnetic declination	Magnetic Inclination	Field strength
Switzerland	Forel, FR	1) 25.XI.21 and 2) 27.VI.22	~ 2.7°	~ 63°	47'950nT
Iceland	Grindavik	30-02.VIII.20	~ -12.5°	~ 75°	52'493nT
Mongolia	Tsenkher	7-12.VI.19	~ -2.9°	~ 68°	59'322nT

Table 3: Summary of the dataset's origin and their corresponding location, magnetic declination, magnetic inclination and total magnetic field strength according to the World Magnetic Model WMM2020 (Ref.6).

Table of the projects properties				
Project	Line spacing	Flying speed	Height (AGL ⁴ /constant)	N° of missions
Forel, FR	1) 5m 2) 5m	1) 9m/s 2) 7m/s	1) AGL 5m 2) AGL 4m	1) 5 2) 7
Grindavik	100m	11m/s	Constant 80masl	7
Tsenkher	50m	10m/s	AGL 45m	10

Table 4: Table of the projects properties: line spacing, flying speed, height (either AGL or constant) and composing number of flight missions.

³ Matlab: engineer and scientist software and programming language used to perform signal processing, data visualization etc.

⁴ AGL : above ground level, surveys with constant separation aircraft-surface

The research projects at each of these places consist of a sum of multiple airborne missions which were undertaken to provide jointly with a magnetic anomaly map as a final result. All the surveys have a corresponding static measurement dataset used for temporal compensation.

The goal of each of the above mentioned research projects was different and will be listed thereafter:

Forel: Project 1) was carried out as a small-scale avant-garde survey (and will be hereafter referred to so) to determine if airborne magnetic measurements could provide quantitative information with regards to UXO position and bulk. A low altitude survey flight was planned in order to detect weak signals. Project 2) was done over roughly the same area 7 months later with a decreased flying speed and altitude.

Iceland: The project was part of a larger geomagnetic observation project which aimed to identify if a magma intrusion (3-9km deep) uplifting a large area was starting to crystallize, therefore becoming magnetic. The flight altitude for this project was held constant at 80m above sea level and very large regional anomalies were the target.

Mongolia: The project was also part of a larger magnetotelluric project aiming to characterize the magma structure of a 50x50km area and up to several kilometers deep for future geothermal development. The geomagnetic surveys were conducted 45m above ground around a geothermal spring to uncover geological features in an area of roughly 4x2km².

4.5 Processing steps

The datasets used to identify outer influences on the measurements from the UAV and the presentation of correction schemes all have common processing steps with varying parameters or steps omissions. In the following, we will briefly review the sequence adopted for the processing applied to the datasets. These steps will be referred according to their number further on.

0. File conversion: The recordings are saved in a .mdd binary file which has first to be converted into a .csv ascii file using a Sensys data tool for further processing with Matlab.

1. Edges cut: First of all, both vectorial datasets (cf. chapter 4.3) are converted into two scalar datasets according to the formula: $B = \sqrt{B_x^2 + B_y^2 + B_z^2}$.

Then, since the recordings always start and finish at the take off position, where the operator manually turns on and off the magnetometer, the extra data needs to be excluded from subsequent processing.

2. Temporal correction: The airborne measurements are subtracted with the base station measurements to remove the temporal variations.
3. Lowpass filter: The next step is to apply a 5Hz low-pass filter that was found to be ideal by Aubert (2019) in removing the noise from the electric motors, the national power grid and the SBB⁵ power grid.
4. Single GPS trace: The GPS measurements from the magnetometer are done at a 5Hz frequency; consequently, they have to be interpolated in such way that every magnetic data point includes spatial coordinates for the centerpoint of the sensor. Then two traces 0.5m left and right from the centerpoint are calculated to account for the exact location of the two traces.
5. Moving mean: This step uses a moving mean spanning over 50 to recalibrate each data point according to the value of its neighbors. In fact, every single data point is added with the 25 preceding data points and the 25 following data points, then the average replaces the data point in question; in the case of Forel 1 this would mean averaging over 2.25m:

$$\frac{200\text{Hz}}{\frac{9\text{m}}{\text{s}}} = 22.2\text{m}^{-1} \rightarrow \frac{50 \text{ samples}}{22.2 \frac{\text{samples}}{\text{m}}} = 2.25\text{m}.$$
6. Decimation: This is the last step that actually performs modifications on the data. The decimation by a factor of 10 is applied to the data. This will smooth the data one more time and preserve one in ten data points to allow higher processing speeds in the visualization step.
- (7. Azimuthal err. corr.): This step is a temporary solution for the heading error correction. It won't be executed for the plot that displays the heading error (cf. Fig.8) but it will be a necessary step to visualize all the other errors on the last plot (cf. Fig.10). Note that for the so-called scalar calibration (discussed in chapter 6.2.2), the heading error correction is performed between processing step 1 and 2.
8. Interpolation: The last step before visualizing the results on a 2D map is called interpolation. Applying this algorithm will artificially create data points between the real ones to fill the voids. The interpolator used for this purpose is a linear triangulation-based nearest neighbor interpolator.

⁵ SBB stands for Schweizerische Bundesbahnen (Swiss federal railways)

9. Plotting scheme: Plots can be created using different color scales and the dynamic range of this scale can be manually adjusted to highlight anomalies, it needs to be chosen carefully in such way that the targets of interest are visually identifiable.

5. Sources of unwanted magnetic influences and other inaccuracies

Chapter 5 describes possible sources of unwanted outer influences, or “errors” occurring in the data, whether they may originate from the hardware, such as the heading error, or the software, such as GPS-positioning related errors or the processing of the traces. We will also have a closer look on the effects of the color scale type and range in the qualitative interpretation of anomaly maps.

5.1 Azimuthal error

One common error in magnetic surveys, whether carried out by land, sea or air is the so-called heading error. This error contains all possible combinations of azimuth, pitch and roll orientation of the sensor and the drone. We will start with the description of the azimuthal error. It is introduced in the data by performing measurements with a setup that doesn't have the same azimuth throughout the whole survey (cf. Fig.4 b). In fact, this will cause the measurements to have a relative difference between each “come” and “go” of up to several hundreds of nanoteslas.

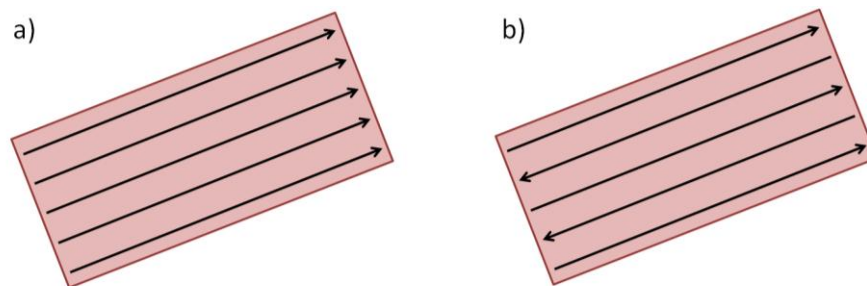


Fig.4 Sketch of two types of surveys with a) identical flight azimuth for the entire survey and with no relative difference in the measurements due to the azimuthal error and b) varying flight azimuth and thus with relative difference between the survey lines of opposite direction, producing a visible azimuthal error in the uncorrected displayed measurements (e.g. Fig.9).

This error is the consequence of the sensor's and the carrier's orientation in space, in this case, the geomagnetometer itself and the UAV. Since both are being exposed to the ambient magnetic field, they will interact with it; the individual response from each material fraction constituting the devices is quantified by its magnetic susceptibility $[\chi]$. This response is characterized by the generation of an induced magnetic field, unique at each inclination and declination of the ambient field, which can alter the real absolute measured value at each position. However, this unwanted influence is negligible due to the fact that little to no strong paramagnetic or diamagnetic elements are present in the sensor and the drone.

The major magnetic influence on the azimuthal error is coming from the permanent (or remanent) magnetization of matter. It is strongest in ferromagnetic materials and consists in a magnetic field imprinted in the material at its solidification stage (at its Curie temperature to be precise) while an

external magnetic field is applied. The remanent field is recorded as a component of the ambient field and in some cases, vectorially adding to it and in other cases subtracting to it.

If the drone was to fly the entire survey with an identical azimuth (and tilting and roll, cf. Fig.4 a), then the error would be constant and could be either disregarded in the case where anomalies are of interest or subtracted in the case where absolute magnetic field values are investigated. However, a perfect constant flight is never achieved in reality due to the relief, wind, GPS inaccuracies etc.

Considering the case of come and goes in Fig.4 b), which is by far the most common survey-type in airborne measurements, because it makes a more efficient use of the aircraft airtime duration and covers more area, we will be required to find a solution to the azimuthal error to show consistent results throughout the entire survey.

To continue, we need to consider another source of error that originates from the manner by which the UAV displaces itself onward in 3D space and keeps a constant azimuth in windy conditions; we will call it the tilting error. The tilting error is part of the heading error and comprises the pitch and roll movements. The heading error could have been handled in one chapter but was split up in two different chapters for the sake of clarity.

5.2 Tilting error

The tilting error comes from the inclination that the UAV requires in order to move in space. To accelerate from the static position (Fig.5 a) to a state of motion, the UAV will vary the pitch and roll angles in the direction it is required to move (Fig.5 b or c). This inclination is limited by the inbuilt software of the M600 preventing it to fly with an angle over 25°.

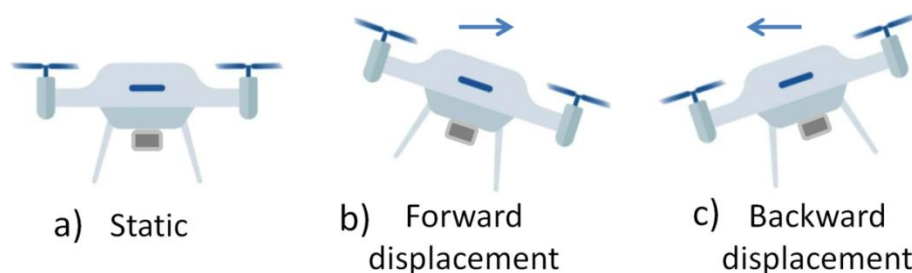


Fig.5 Sketch of two types of UAV displacement using tilting, where the UAV shows in a) no displacement, b) a forward displacement following the tilting and c) a backward displacement for the same reason. The ambient magnetic field will induce different magnetic fields for a), b) and c) that will in turn impact the measurements in different ways. This is the reason why we need to correct for the tilting error.

Equally as for the heading error, the error introduced by the tilting doesn't affect the results as long as the tilting remains identical throughout the whole survey, i.e. as long as it remains a constant.

However, this is in reality never achieved because the UAV needs to accelerate from a static position to gain speed and then reduce its tilting because no further acceleration is needed but only the maintaining of a set constant speed (for most types of geomagnetic surveys, to keep a homogeneous spatial sampling, the acquisition/flying speed should remain constant). The UAV also needs to tilt itself backwards (Fig.5 c) at the end of the survey lines and to decelerate before performing the U-turns in order to continue with the next survey line in opposite direction. In addition to that, wind gusts affect the inclination (both pitch and roll) of the UAV for the reason that, when operated in automated mode, it is programmed to follow on a specific track and thus compensate for relative medium displacement and GPS offset position. These variations in inclination produce the tilting error in the data which can be in the order of a few nanoteslas [nT]. These undesirable artifacts can be misinterpreted and will have to be corrected for.

Now if we consider both the azimuthal and the tilting error as a single one called heading error, as mentioned earlier, we do in fact end up with a problem that is almost identical to the one encountered by nowadays smartphones and satellites fluxgates magnetometers. We will see later how this similarity can provide useful insights for calibration algorithms.

5.3 Positioning related errors

Automated surveys can be designed with a certain number of waypoints that the UAV uses as reference for its flight. In fact, the UAV will fly in straight lines between each waypoint and satisfy every one of them. The constructor of the M600 limited the UAV's internal software to a use of 99 waypoints for any continuous flight mission. If a survey is designed with more than 99 waypoints, the UAV will follow the programmed route and simply stop at the 99th. After this, it will require to hover/stand again at close range from the pilot to load and complete the rest of the mission. Consequently, it is impossible to perform one large continuous mission in one flight even though the UAV's batteries could last for that entire mission. This forces the operator to design smaller missions, especially if the relief is rugged and not constant as above a lake, therefore requiring a greater number of waypoints to accurately follow the terrain. Keep in mind that for very rugged terrain, the programmed speed of flying should be proportionally decreased such that the latency due to the UAV's momentum is not a source of inaccuracy.

In the case of the M600, one part of the error comes from this limited number of waypoints. In fact, the more waypoints are used to define the track of the UAV, the more precise will be its terrain following precision. On the other hand, the fewer waypoints are used to define a complex flight path, the greater the inaccuracies with respect to the altitude above ground. Since we want to avoid as much as possible complex topography corrections, we need to ensure an acceptable threshold. In the mission planner software, UgCS (cf. chapter 4.2), we can define the tolerance for the above ground level

altitude (AGL tolerance). It is usually set to a value below 1m. The software then distributes the waypoints in the predefined zone within this tolerance. This way, we can optimize the use of the waypoints to cover as much area as possible within one single mission at the cost of a controlled inaccuracy.

On top of this inaccuracy, the actual waypoints are placed over a digital terrain model which is itself an approximation of the terrain in reality. Yet the flight path, as precise as it might be with respect to the planned mission, will only be as accurate as the digital model terrain used in its planning. The error deriving from this imprecision depends on the loaded digital terrain model. The mission planner comes with a pre-loaded satellite elevation model called SRTM-4 void-filled elevation data. The resolution of the SRTM-4 is 90m at the equator (30m but not for all countries, cf. SRTM v4.1 digital elevation database 2022). According to Mukul (2017), “The Shuttle Radar Topography Mission (SRTM) Digital Terrain Elevation Data (DTED) are used with the consensus view that it has a minimum vertical accuracy of 16m absolute error at 90% confidence (Root Mean Square Error of 9.73m) world-wide”.

Now if we move on to the ability of the UAV to follow a track, we need to have a look at its positioning system, in this case it is a triple redundant global positioning system (GPS). It would be pretentious to assume that the actual flight is as straight as initially programmed between each waypoint; as a matter of fact, variations of up to a few meters (cf. Table 5) have to be expected due to inaccuracies in GPS-positioning.

DJI GPS properties	
N° of GPS (redundant)	3
Lateral accuracy	1.5m
Altimetry accuracy	0.5m

Table 5: Summary of the lateral and vertical accuracies of the DJI GPS as given by the constructor.

As can be seen on Table 5, the altitude accuracy is lower than the lateral one. This is achieved thanks to the added barometric sensor combined with the GPS altitude data. As we will see later, the correction for this error is until now unfeasible because the absolute position of the UAV at each measurement position needs to be known. However, the artifacts derived from this error can be visually identified by an expert’s eye. In fact, the anomalies produced by a higher altitude error have the common signal signature of being wider, elongated and weaker than at the correct altitude. On the other hand, the anomaly errors derived from shallower altitude have the common signal signature of being narrower, spikier and with higher amplitudes.

If the survey type is low altitude and the targets are weak anomalies, the interpreter may visually identified both of the above mentioned signal differences by comparing the suspected tracks with neighboring survey lines to see whether they do or do not show similar patterns.

Besides UAV track-related inaccuracies, the actual measurements are tagged with GPS coordinates from the MagDrone R3 device itself. The sensor has an in-built GPS which records at a rate of 5Hz the coordinates with a timestamp as well as the number of satellites and a GPS quality indicator.

Sensys GPS quality indicator	
Value tag	Expected accuracy
1 = 2D/3D	4-6m
2 = DGPS	1-3m
4 = fixed RTK	0.01-0.05m
5 = floating RTK	0.2-0.4m
6 = dead reckoning	for urban areas

Table 6: Summary of the properties of the Sensys MagDrone R3 GPS as given by the constructor. All the missions used in this work had the DGPS tag.

As can be seen on Table 6, the quality indicator of GPS coordinates from the geomagnetometer can vary from 1cm to up to several meters, depending on the number of satellites, their geometry, and the presence or not of RTK signal. For all the datasets used in this research, the GPS signal tag was 2, corresponding to the DGPS (Differential GPS) which means that the device attributed coordinates within an accuracy of 1 to 3m to the data points.

Positioning related errors	
Error source	Impact
Waypoint maximum number	Limits the size of the survey according to the AGL tolerance, particularly when the terrain is rugged.
Digital model terrain	Controls the inaccuracy of the planned flight path.
GPS of the M600	Introduces inaccuracies of up to 1.5m laterally and 0.5m vertically.
GPS of the magnetometer	Depends on the quality of the signal with an accuracy range from 1cm to several meters.

Table 7: List of the discussed topography related errors and their impact on the measurement positioning.

Finally, Table 7 sums up all the positioning related sources of error and their respective impacts in terms of accuracy. We can see that, in the worst case, the summed up inaccuracies can reach several decameters. Even so, survey projects such as the ones conducted in Tsenkher (Mongolia) or Grindavik

(Iceland) wouldn't have been strongly impacted by deviations of <10m for the reason that large regional anomalies were targeted at high altitude and not smaller more subtle ones such as UXO, were not only the detection itself of the anomaly is essential but also its accurate location.

Nevertheless, outliers in measurement position can still be visually identified, we will see later how with examples and by what method to minimize this inevitable imprecision.

5.4 Dual sensor differences

Equipped with two fluxgate-type 3-axial sensors separated by 1m, the geomagnetometer should provide with two close to identical datasets in the case where the flight altitude is much larger than the sensors spacing. However, this is very rarely observed because the device is attached to the landing skid of the UAV, very close to the main frame and brushless motors⁶ which have induced and permanent magnetic fields that influence the total recorded field. Said difference among sensor 1 and sensor 2 is per se not an error directly but an unwanted magnetic difference that will be subject to the calibration that will take place later on, attesting of its efficiency and validity.

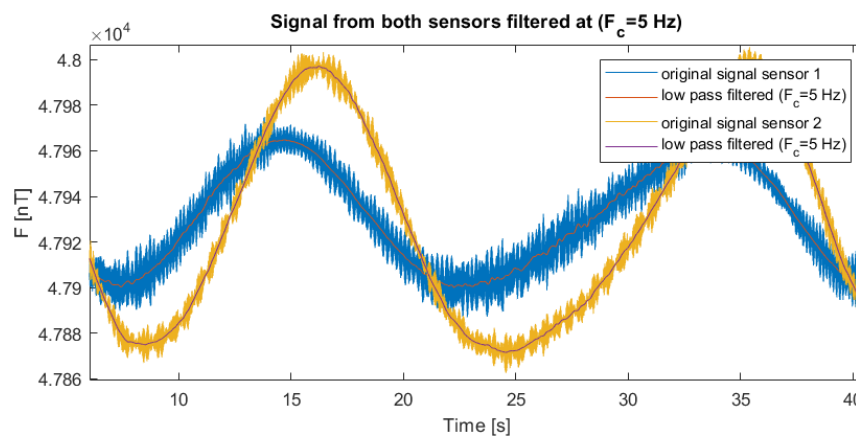


Fig.6 Signal of both fluxgate sensors (sensor 1 in blue and sensor 2 in yellow) that underwent the processing steps 0 to 3 (chapter 4.5). The 5Hz cutoff version from Sensor 1 is in orange and sensor 2 in purple) from the geomagnetometer after performing twice 360° rotation at the same position over the area of investigation in Forel, at ~100m above ground.

The influence of the remanent magnetic fields can be observed on Fig.6 which represents the signal recorded when the UAV performed two 360° rotations at a stable position 100m above the Lake of Neuchâtel for the Forel avant-garde research. As we have seen in Table 3, the Earth's magnetic field strength over Forel is ~47'950nT. This is close to the mean of both signals, proving that our measurements are, for this case study, consistent and in agreement with the true expected magnetic field value.

⁶ Brushless motor: type of electrical motor using purely induction to rotate without carbon-contacts as for brushed types.

The first rotation and also the more symmetrical one was completed between the time interval 5-25s (Fig.6). Signal 1 and 2 show a phase shift of around 2.5sec, which corresponds to 45°. The dynamic range of the two signals isn't equivalent for both signals. Signal 1 has a dynamic range of ca. 60nT, whereas signal 2 ca. 125nT. The difference is around 65nT, more than twice the dynamic range of signal 1. A possible cause for this difference can be the not perfectly centered sensor position on the UAV, which is attached by the operators.

In order to better constrain the cause of this amplitude difference, the magnetometer should be mounted on the UAV and used to perform an automated mission with a 360° rotation at the same position (pure azimuthal variation). Then, the magnetometer should be mounted in reverse, i.e. with sensor 1 in place of sensor 2 and vice versa. If the amplitude of signal 1 matches the amplitude of signal 2 in the second survey and vice versa, then the above mentioned difference is likely due to the static magnetic fields of the UAV and the off-centered position of the sensor.

The difference of dynamic range mentioned above was a problem encountered and corrected by Aubert (2019) by calculating the mean of both signals and the processing carried on with one single trace. For high altitude missions such as in Tsenkher (Mongolia) the additional information that two traces separated by 1m offer have no direct benefit. This procedure also had the advantages of being rather straightforward and resulting in faster operation. The downside is for close to the ground surveys because the duality of the measurements is lost, i.e. that one single average signal was centered on the flight path instead of two split up by 1m, in other words 50cm left and right from the flight path.

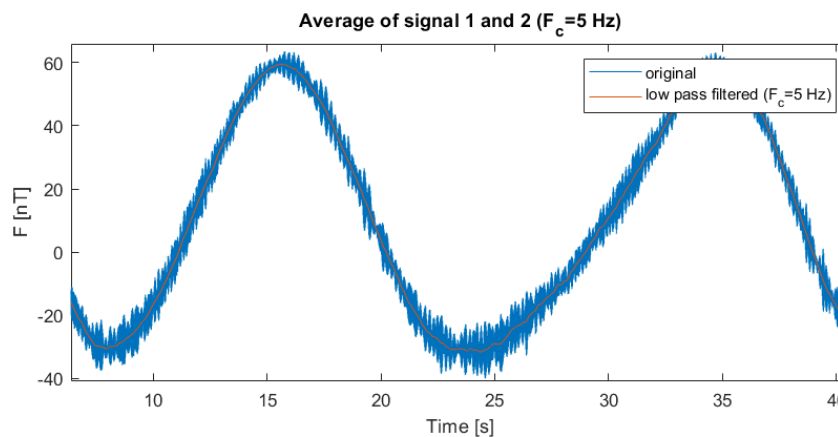


Fig.7 Same period and processing observed as Fig.6; average of both fluxgate signals from the geomagnetometer (blue curve) and its 5Hz cut-off version (orange curve) after performing twice 360° rotation at the same position over the area of investigation in Forel, at ~100m above ground.

The mean of both signals (in blue) is showed in Fig.7 along with its low pass filtered version (in orange). The signal strength scale is given in relative values to better visualize the total amplitude difference. From the low pass filtered signal (in orange) it can be observed that the heading error can

produce signal amplitude differences of up to $\pm 45\text{nT}$ between two profile lines. This value exceeds most of the UXO anomalies that we wish to detect at 5m of height above the ground; consequently it is an error that we will need to correct for.

5.5 Color coding of data

Another crucial step that can lead to misinterpretations is the type of color scale and its values range (Cramer 2020). In fact, Matlab has a wide variety of color scales available with different color transitions and patterns. In the case of archeological geomagnetism, the color scales are usually black and white for positive and negative anomalies, or vice-versa. This helps the interpreter to quickly identify features such as buried walls or old fireplaces. However in the field of planetary geomagnetism, it is more usual to witness rainbow maps representing positive and negative anomalies in red and blue respectively.

On top of the choice of the color scale lies the choice of the actual range of values. Geomagnetic datasets may contain outliers that are, after the processing described in chapter 4.5 normally damped, but very strong anomalies may still have outliers that will pull the range of values at one extreme or the other and thus expanding the color distribution of the scale and in this way making other anomalies less to not visible at all. It is always important to keep an eye over the numerical results while creating an anomaly map.

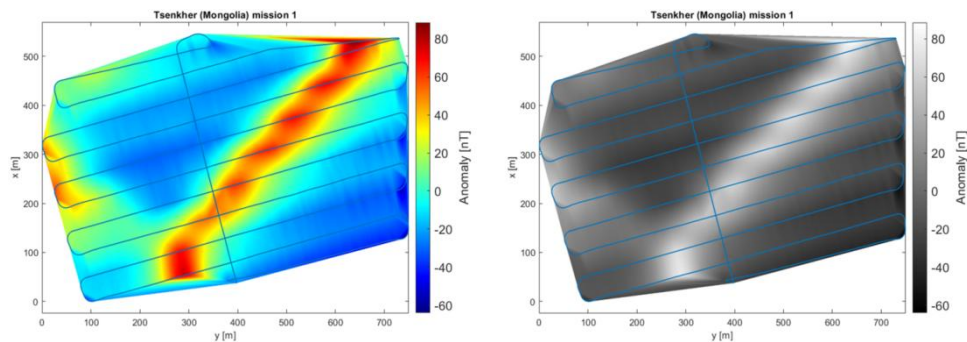


Fig.8 Comparison of different color scales using mission 1 from the Tsenkher (Mongolia) project. The blue track represents the drone’s path with a transversal line in the middle to have reference points. This data underwent processing steps 0-8 described in chapter 4.5. Step 9 is the only differing in both plots. Left, a rainbow (“jet”) scale with the 0 being in the turquoise color region. Right, identical dataset plotted in a black-white scale with 0 being in the gray region.

To compare the rainbow and black-white color scales, a dataset from the Mongolia project in Tsenkher was used. The dataset was processed using the processing steps described in chapter 4.5 (0-8), the last step (9) was the only one differing to create both plots shown in Fig.8. The “jet” color scale plot tends to over-emphasize lateral contrasts whereas the black-white color scale plot tends to make the anomaly in this example less straightforward to identify. The black and white plot tends to only make dominant

anomalies eye-catching, as for the “jet” colored plot the entire close to 0-valued region (turquoise-green-yellow) also appears eye-catching which could induce over-interpretation. More of these comparisons will be presented in the chapter 6.4 as well as their advantages and disadvantages.

5.6 Case in point from Forel

In the following we will review one survey mission from the Forel project that highlights the above described magnetic influences and interferences that require correction and calibration. The same dataset will be plotted twice, once to show up the azimuthal error and a second time with a correction factor applied to remove the azimuthal error to display the features of the other errors. As mentioned in chapter 4.4, the goal of the Forel survey was to identify potential zones containing UXO as a small avant-garde project, the flight was therefore low (5m above the lake surface) and dense (5m spacing).

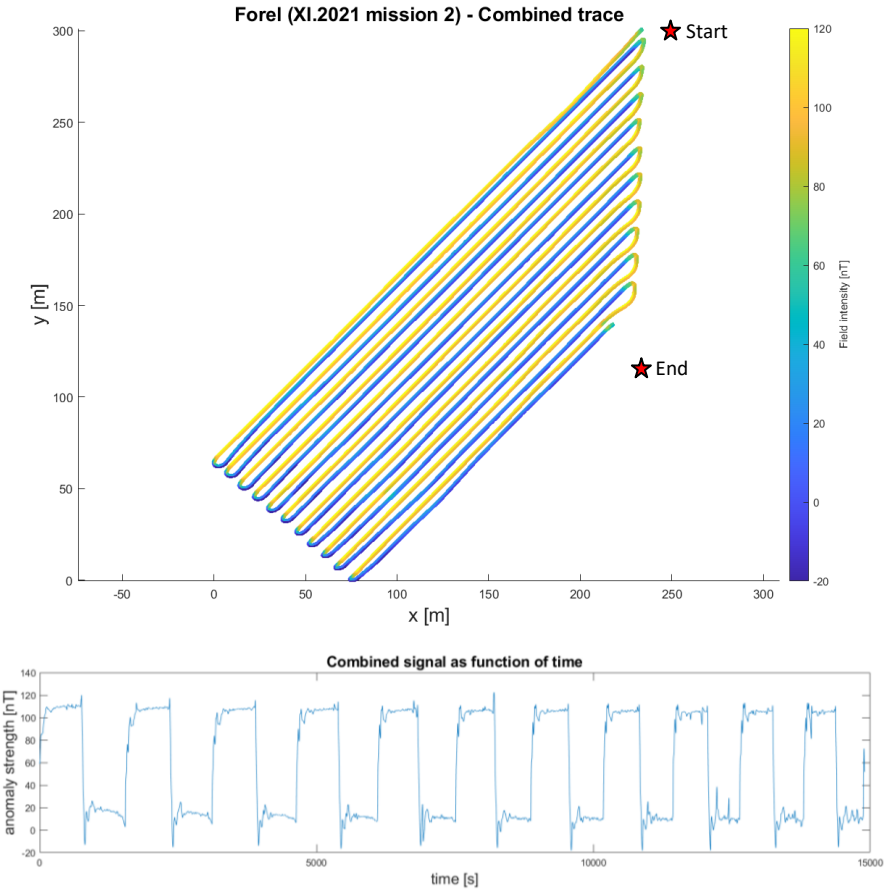


Fig.9 Both plots show the Forel avant-garde raw data as collected by the drone. The data underwent all the processing steps from chapter 4.5 with the exception of the heading error and interpolation (step 7 and 8). The upper plot is a 2D spatial plot out of which no realistic quantitative interpretation can be done because of the azimuthal error, which makes the lines appear successively yellow and blue. The plot below is the signal from sensor 1 as a function of time; it resembles a periodic square-function which is due to the azimuthal error where each peak and trough corresponds to the odd and even come-and-go lines.

As mentioned above, we will first review the azimuthal error and conclude this chapter with an overview of the rest of the errors. The processing steps applied to the dataset to acquire the anomaly map in Fig.9 include step 0-9 (cf. chapter 4.5) without the azimuthal error correction (step 7) and interpolation (step 8). It appears obvious that the azimuthal error overprints the data of interest and makes it impossible to render a qualitative interpretation of potential UXO without applying a correction scheme.

One way to correct for this error is to find the mean of each trace and subtract it from the signal, generating thus a signal oscillating around 0 which will help for characterizing positive and negative anomalies. Then, the mean of all the positive parts of the signal must be found and subtracted to it again. Idem must be done for the negative part of the signal. Table 8 shows the compensations procedure applied to each of the traces.

Temporary heading error compensation			
Trace	Condition	Statement	Dynamic range
Trace sensor 1	If the values are positive	Apply -57.03nT compensation	117.40nT
	If the values are negative	Apply +60.37nT compensation	
Trace sensor 2	If the values are positive	Apply -31.32nT compensation	65.92nT
	If the values are negative	Apply +34.60nT compensation	

Table 8: Temporary procedure for the compensation of the heading error. This correction serves the only purpose to display the other errors on Fig.11. The resulting signal after the compensation was applied is shown on Fig.10.

Once again, we can see in Table 8 that both sensors do not share similar amplitude errors for the azimuthal correction (cf. chapter 5.4). To visually judge if the compensation is satisfactory, it is plotted on Fig.10. Ideally, the mean throughout the survey should be around 0. The compensation was judged to be acceptable if the delta-peak looking spikes are ignored. These spikes are due to an over-compensation happening whenever the UAV performs U-turns.

This correction method is naturally suboptimal because it assumes that the tilting of the UAV is constant throughout the mission. Therefore, the U-turns are not corrected according to the true azimuth of the UAV. Furthermore the data associated with these U-turns will make the signal mean deviate from the corresponding true survey-line mean. However, this method was judged acceptable to present the other errors in a visible way: Fig.11 shows the spatial map corresponding to the signals plotted in Fig.10.

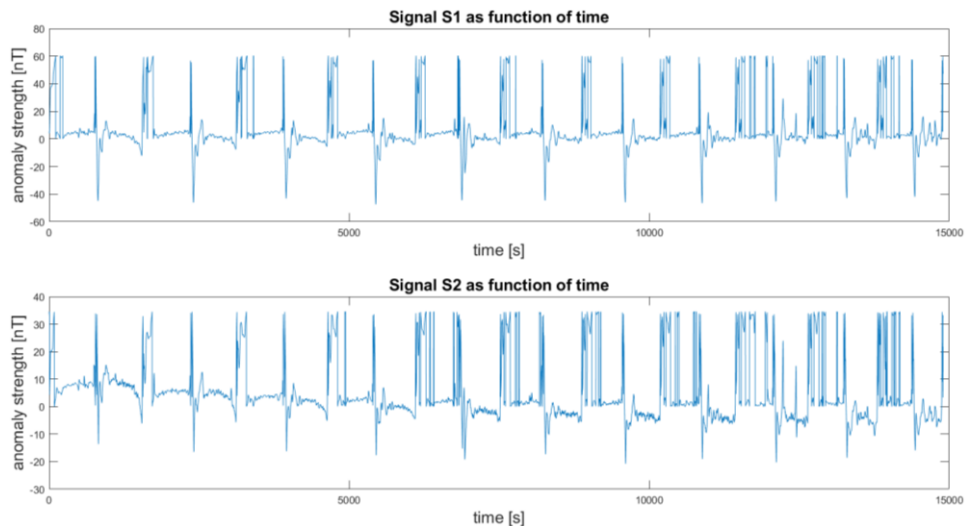


Fig.10 Plot of the heading error corrected signal from the sensor 1 and 2. The remaining noise in the form of delta spikes occur at each U-turn the UAV performs, modifying its tilting angle which in turn affects the magnetometers recordings.

On the upper left corner of Fig.11 we have an example of tilting errors. This happens, among others, after the UAV performs a U-turn and has decreased its speed and tilting (first red frame at the bottom), it then needs to regain speed up to 9m/s (second red frame) and will slightly surpass this speed and again slightly swing back (third red frame) before maintaining the correct speed which does not require further tilting changes.

On the upper right corner we can see how positioning related errors may affect the results by incorrectly geo-referencing the data; in this case, this error is visually identified by the line separation of 5m which is narrower between the two first lines. We cannot say without the logs from the UAV if this error was due to an inaccuracy of the sensor's GPS, or an inaccuracy of the positioning of the UAV relative to its flight path, or a combination of both.

On the lower right corner we can observe the dual sensor differences over some anomalies that only appear in the data of one sensor for odd lines. If the data were interpolated we would see anomalies cut in half due to this.

Finally, on the lower left corner we see a U-turn which displays artifacts (here fake anomalies) due to the tilting and azimuthal error summed up together, called the heading error. It seems that all the U-turns strongly affect the data at these specific locations (as was shown in Fig.10) and should be discarded from the anomaly maps if not corrected.

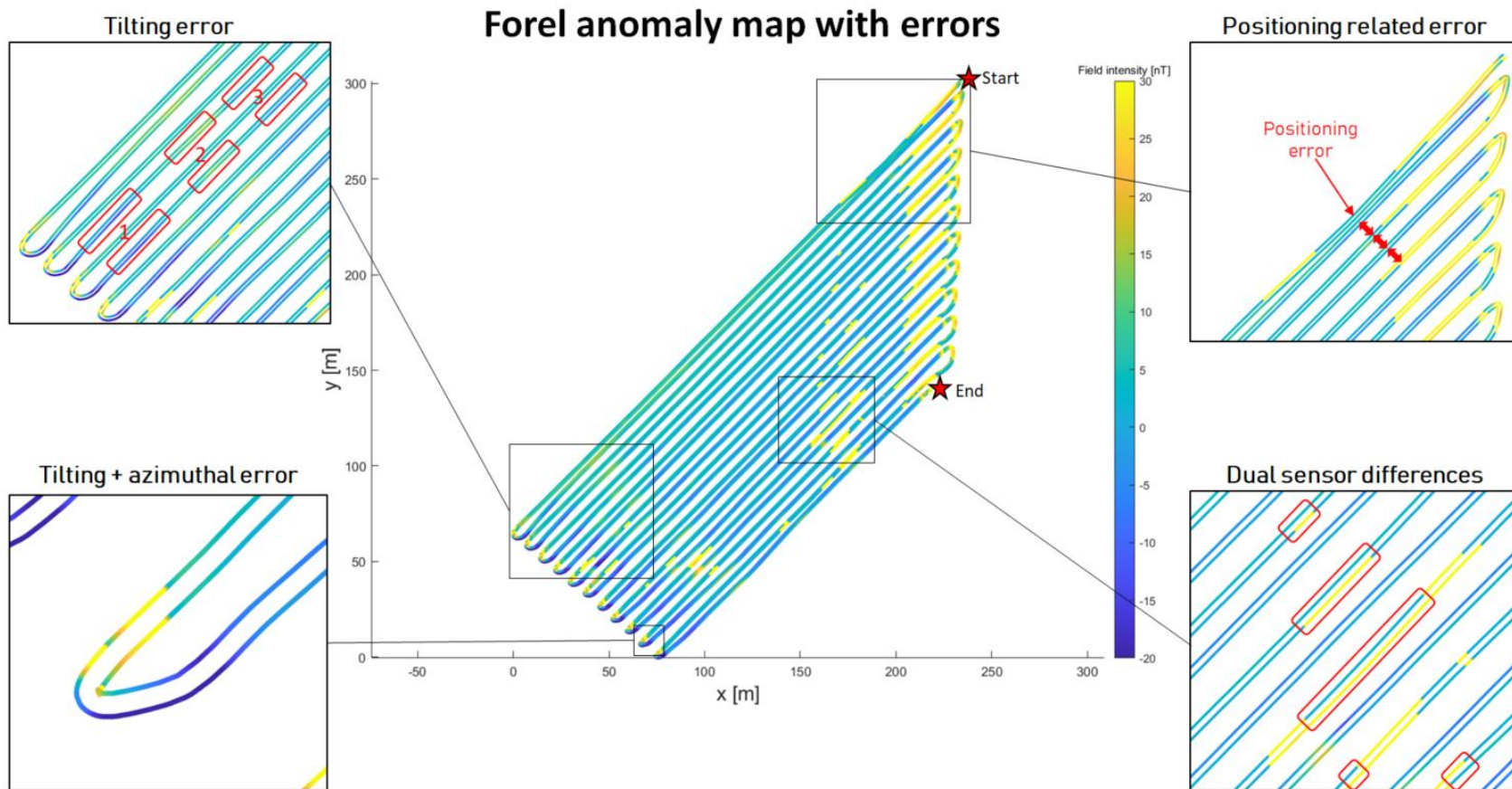


Fig.11 Plot of mission 2 from the Forel avant-garde project (cf. chapter 4.4 Datasets) that underwent all the processing steps mentioned in chapter 4.5, including the temporary heading error correction. The resulting map as such presents most of the discussed errors in chapter 5. The tilting error (upper left corner) occurs when the UAV changes its tilting, on the zoom-in figure, we can identify “fake anomalies” (red rectangles) resulting from the swinging effect due to the UAV’s speed changes. The positioning related errors (upper right corner) show the two first come-and-go lines with very little separation, for comparison, the other lines have 5m spacing (smaller red arrows). The dual sensor differences (lower right corner) can be sharply recognized in the red rectangles where one sensor appears to have neutral values and its vis-à-vis counterpart relatively higher values. It seems to be the case only for odd lines. Finally, the tilting and azimuthal errors are jointly visible (lower left corner) when the UAV performs the U-turns, again strong “fake anomalies” are present at every sharp turn the UAV performs throughout the entire mission.

6. Development of correction techniques

This chapter will focus on the correction techniques and methods that we can apply to the survey design, the equipment, and the processing of the datasets to ensure the highest reliability possible and enable qualitative interpretation.

6.1 Survey design

The survey design will depend on the target size and its signal strength. For projects such as the ones in Mongolia or Iceland, the objective was to explore and uncover large geological structures such as faults and petrological units. In all the cases, the survey-type should be a raster optimized for airtime such as discussed in chapter 5.1. To be defined are the flying speed, height and line spacing that will be discussed in the following.

In the case of surveys for geological exploration, usually larger areas with survey tracks up to a few hundred meters need to be covered. This involves altitude flights of up to hundred meters above the ground with line spacing of similar size at potentially higher speeds ($>10\text{m/s}$). In fact, the line spacing should be equal to the altitude above the ground no matter what type of target is being surveyed. This way of proceeding is a good compromise between sufficient lateral covering and speed of acquisition.

In the case of surveys where a particular structure or object is investigated, most of the time, there is already an idea of the associated signature, and the survey can be designed at an altitude where the signal strength still appears clearly in the data.

In some other cases, the object or anomaly's signature isn't a priori known and the survey has to be conducted with compromises, where the survey area and resolution are inversely correlated in the case of identical dedicated time for the missions. If time is not a limiting factor, then the highest resolution should be chosen, keeping in mind that the UAV is physically limited to flying at shallow heights above the ground to avoid collisions; this limit will usually be in the order of a few meters, thus the line spacing too.

Finally, in some other cases, the object's signature isn't strong enough to produce a perceptible signal at the sensor's lowest height. This case is the worst-case scenario, because the absence of the object's signature in the data will be interpreted as an absence of the object itself. If the object is the target, then the area that is being investigated will be enlarged and this situation will promote further surveying in the neighboring zones with little chance of success if the already surveyed area was discarded.

On top of the conventional raster survey design, there should be at least one transversal line (cf. Fig.8), ideally 3 (one in the middle and one for each side of the survey), in order to have multiple points in space with two measurements at different azimuth and time. These points will be called reference

points and will be used in the final stages of the processing as quality control points to verify that the corrections were appropriate.

The datasets presented in chapter 4.4 have all been acquired with a UAV heading forward and rotating (yaw) to keep the head of the UAV pointing in the direction of movement. This induced the so-called azimuthal error. In chapter 5.1 (Azimuthal error) the raster survey of come-and-go type was discussed to be ideal for airborne measurements, but there could be another way of operating the UAV such that the UAV's front always points toward the same azimuth. This possibility will be called the constant yaw solution.

The constant yaw solution's aim is to get rid of the heading error by keeping the azimuth of the UAV constant. Although this may seem an uncommon way of flying (cf. Fig.12), it is totally feasible from a soft- and hardware's perspective. However, the UAV will still experience the tilting error which is a component of the heading error (cf. end of Chapter 5.2).

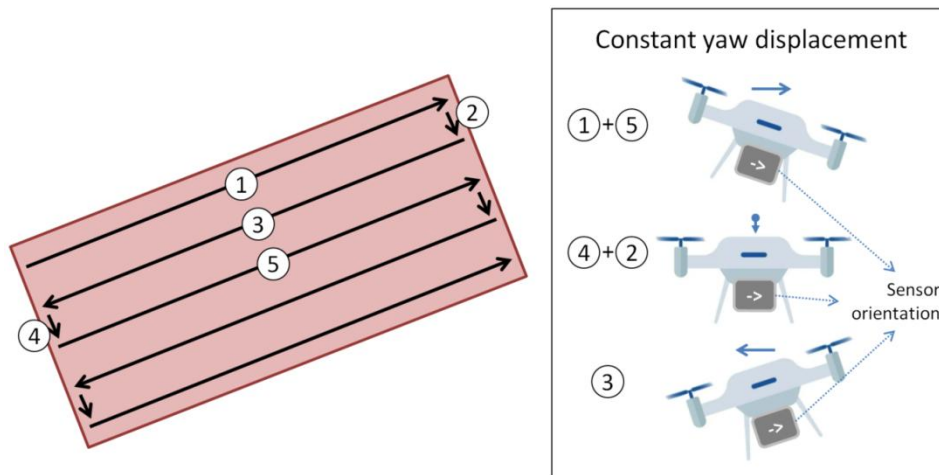


Fig.12 The survey design “constant yaw displacement” assumes that the UAV will fly in all directions while keeping its azimuth constant. The first profile line 1, starts with the UAV tilting forward and displacing itself forward (note that the sensor orientation keeps pointing towards the right at all flying directions). Then the second line 2 is completed with a lateral displacement, but the sensor still points to the right. The 3rd line consists of backward flying of the drone, because the sensor still points to the right. And finally, line 4 and 5 are the same as 1 and 2 respectively.

Actually, it is less complicated to look at the azimuthal and tilting error as one single problem (called the heading error) instead of two, which will be subject of the next chapter. Once this error is corrected, the flying azimuth of the UAV will not matter, and the type of survey (heading forward or constant yaw) will be irrelevant for the quality of the results.

6.2 Heading error solution

Previously named after the combination of both azimuthal and tilting error, the heading error comprises all possible sources of error that originate from the sensor itself, its apparatus and its carrier. Since the MagDrone R3 sensor was designed for airborne applications, its carbon-composite frame makes it lightweight and has the property of being very little diamagnetic, whose contribution to the total magnetic intensity (TMI) is negligible.

6.2.1 Distant sensor solution

One solution to the heading error, considering that the sensors apparatus doesn't alter the magnetic measurements could be to place the sensor as far as possible from its carrier, here the UAV. In fact, the signal amplitude is inversely proportional to the distance squared ($F \propto \frac{1}{r^2}$). This means that in the case of amplitude variations of ca. 100nT (cf. Table 8) and an acceptable residual force of ~1nT, we would need the signal strength to drop by 100 times; this corresponds to a separation sensor-UAV 10 times larger than it currently is. In other words, the sensor would need to hang around 3m below the M600.

This setup has been successfully implemented by Parshin et al. (2018), in the case of hanging magnetometers and Macharet et al. (2016) for fixed magnetometers on a special arm, 1m ahead of the rest of the chassis (cf. Fig.13).

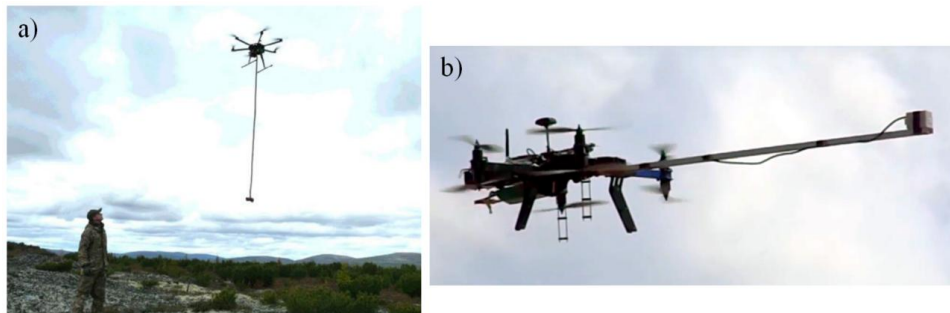


Fig.13 Representations of successful solutions to the heading error consisting in separating the magnetometer from noise sources (i.e. the UAV itself) as much as possible. a) proton magnetometer held 3m below the UAV (Parshin et al., 2018); b) fluxgate magnetometer held 1m in front of the UAV with a special frame extension (Macharet et al. 2016).

In our case though, for safety reasons and to avoid additional swinging and positioning errors, the sensor was decided to be kept firmly attached to the landing skid of the M600. This greatly simplifies take offs and landings plus allows the UAV to fly at higher speeds in windy conditions because the sensor won't swing.

Instead of dealing with the azimuthal and tilting error separately (cf. end of chapter 6.1), it was decided to correct the heading error with one single solution described by Olsen et al. (2003). This solution is called magnetic compensation or scalar calibration; it achieves better results than the manual compensation of the heading error (cf. Table 8) and doesn't require the log data from the M600 alongside complex flight analysis to recover the tilting at any measurement position. The magnetic compensation accounts for errors that may appear in the form of remnant magnetization, induced magnetization, and eddy currents, classified in Table 9.

6.2.2 Scalar calibration and compensation for magnetization

Munsch et al. (2007) showed that fluxgate magnetometers can be calibrated with a rather simple procedure in the field and that this calibration simultaneously accounts for the remnant and induced magnetization of the equipment with a standard deviation of 1nT for hand-held surveys with fluxgate-type geomagnetometers. The calibration scheme was adapted from Olsen et al. (2003) who developed it in order to calibrate the magnetic measurements of the SWAR satellites.

3D orientation errors		Solution
Error name	Error description	Solution name
Calibration	Error from the calibration of the sensor (sensitivity, offset and non-orthogonality angles)	Scalar calibration
Induced magnetization	Induced magnetization from the apparatus (i.e. components of the MagDrone, frame, battery etc.)	
	Induced magnetization from the carrier components (i.e. parts of the M600 such as frame, batteries, electronics etc.)	
Remnant magnetization	Remnant magnetization from the apparatus (i.e. components of the MagDrone, frame, battery etc.)	
	Remnant magnetization from the carrier components (i.e. parts of the M600 such as frame, batteries, electronics etc.)	
Eddy currents	Eddy currents in the apparatus	
	Eddy currents in the carrier	

Table 9: List of the 4 categories of errors relative to the sensor, its apparatus and the carrier (UAV) alongside their respective solution.

On top of the remnant and induced magnetizations another type of error can appear, called Eddy currents, and it happens in all materials that undergo fluctuations of ambient magnetic fields. They

consist of electrical currents induced by changes in the ambient magnetic field, which in turn generate secondary magnetic fields that can impact the recordings. This happens while the drone is flying through magnetic fields with varying intensity. Since the only strong varying magnetic fields happen to be the electric motors, they are easily filtered out with a low pass filter (chapter 4.5 step 3).

To compensate for the earlier mentioned magnetic moments, a scalar calibration will be required. This procedure was initially described by Olsen et al. (2003) for satellite geomagnetometer calibration and is identical for UAV's calibrations. This procedure requires a dataset containing enough random 3-axial measurements in as many azimuthal and tilting combinations as possible at one position to perform an estimation of 9 correction parameters through a linearized least-square inverse problem.

According to Munsch et al. (2007), the magnetic field vector $B (B_1, B_2, B_3)^T$ is connected to the output of the magnetometer $F (F_1, F_2, F_3)^T$ via:

$$F = S \cdot P \cdot B + O \quad (1)$$

where:

- S is a 3x3 matrix containing the sensitivities (i.e. the weights) and is assumed to be diagonal.
- P is a 3x3 matrix containing the angle in $[\circ]$, which are obtained by the transformation from the magnetic field vector B into a new vector such that the coordinate system specific to the sensor is respected. It is assumed that the 1st axis is projection invariant, thus $= (1 \ 0 \ 0)$, that the 2nd axis has one degree of freedom (u_1) and that the 3rd projection axis has 3 degrees of freedom (u_1, u_2, u_3).
- O is a vector containing the offsets (or the constants) for each axis.

Equation (1) then rewrites:

$$\begin{pmatrix} F_1 \\ F_2 \\ F_3 \end{pmatrix} = \begin{bmatrix} S_1 & 0 & 0 \\ 0 & S_2 & 0 \\ 0 & 0 & S_3 \end{bmatrix} \cdot \begin{bmatrix} 1 & 0 & 0 \\ -\sin(u_1) & \cos(u_1) & 0 \\ \sin(u_2) & \sin(u_3) & \sqrt{1 - \sin(u_2)^2 - \sin(u_3)^2} \end{bmatrix} \cdot \begin{pmatrix} B_1 \\ B_2 \\ B_3 \end{pmatrix} + \begin{pmatrix} O_1 \\ O_2 \\ O_3 \end{pmatrix} \quad (2)$$

Olsen et al. (2003) also included additional parameters for the correction of temperature and time (aging factor) in the equation but were neglected by Munsch et al. (2007) and will be hereafter identically neglected considering that they are only relevant for satellite missions of several years with temperature amplitudes of the order of tenth to hundredths of degrees Celsius.

Given that we are looking for the magnetic field B , equation (1) rewrites:

$$B = P^{-1} \cdot S^{-1} \cdot (F - O) \quad (3)$$

The solution of this problem consists in minimizing the weighted least square χ^2 (Munsch et al. 2007):

$$\chi^2 = \sum \left(\frac{B - M}{\sigma_B} \right)^2 \quad (4)$$

where:

- M represents the measured and transformed values of the magnetic field.
- σ_B is the data errors (here artificially set to 1).

The above-described scalar calibration procedure is based on two assumptions; the first one is that the true magnetic field intensity is known at the location of the calibration and the second one is that the disparity between the measurements and the real absolute value is only due to the magnetometer device and carrier and not any other external influence. This is why it is also important to remove the temporal variations of the dataset.

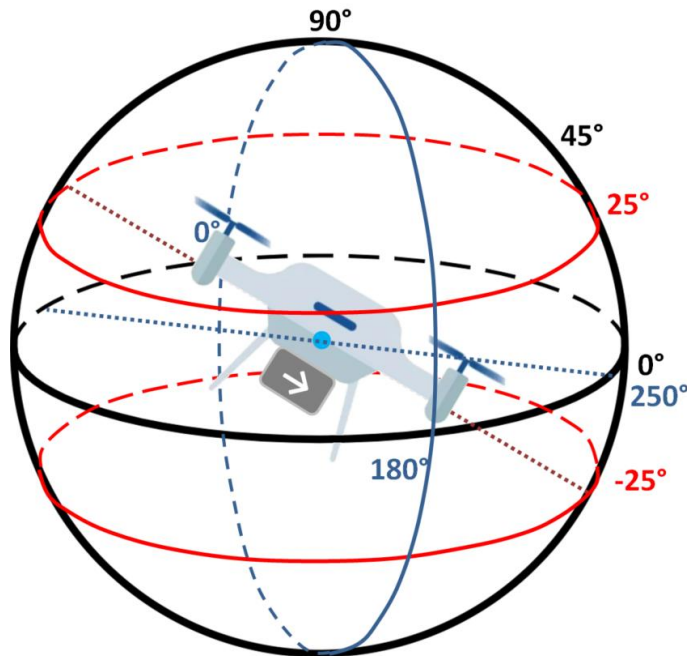


Fig.14 Sketch representing the UAV tilting with -25° to the right (brown dotted line) with a direction of ca. 250° (blue dotted line). The red longitudinal lines ($\pm 25^\circ$) on the sphere represent the maximum tilting angle allowed by the software of the M600. The UAV can rotate from 0° to 360° without restriction with an axis perpendicular to the equatorial plane.

As for satellites, the UAV can move in space in all possible orientations (theoretically). Though in our case, the constructor of the M600 limited its tilting (pitch and roll) to a maximum of $\pm 25^\circ$ (cf. Fig.14) with respect to the horizon. For the scalar calibration the used dataset requires that the UAV varies its attitude⁷ as much as possible in one place and orient itself randomly in order to cover as much combinations as possible. The problem is that the UAV cannot perform acrobatic maneuvers such as

⁷ "The orientation of an aircraft or spacecraft, relative to the direction of travel" Oxford languages

flips because of the above mentioned limit; this will be a limitation in the generation of random data for the scalar calibration.

Nevertheless, the tilting limit of the UAV will not negatively impact the scalar calibration because the UAV will not be autonomously flying beyond these pre-programmed limits during the survey missions anyway.

6.2.3 Algorithm development

The development of the algorithm to minimize the least-square misfit χ^2 (4) was performed using Matlab. The script and functions to perform the search of the 9 parameter values can be found in the Appendix 9.1 to 9.3 and its corresponding flow chart is shown in Fig.15. When fully run, the script yields in the end values for each of the 9 parameters mentioned above. These are used later in the processing of the survey data to calibrate and compensate the missions.

The script is sub-divided in 3 main parts:

1. Preliminary: In the first part of the code the user should load the raw dataset containing exclusively the random measurements already clipped from the unwanted take-off and landing measurements. It is also required to provide the absolute value of the Earth's magnetic field (variable called B) at the position of the calibration in the field. Keep in mind that this value doesn't affect the final results as long as relative field variations are of interest and not absolute field values.
2. Loops: This part contains the core of the algorithm which consists of one loop inside another larger one whose goal is to minimize the least-square misfit (variable named χ^2). The inside (also called secondary) loop goes iteratively through all nine parameters and observes by calculating two χ^2 if increasing the parameter or decreasing it (by a given step length) results in a lower or larger misfit (χ^2).

Then, the parameter that produced a smaller χ^2 is updated and the loop continues with the next parameter until all nine are visited. If both values generated χ^2 that were larger than the one in the previous loop, it means that the minimum was over-jumped and the step factor is divided by 10 in such way that in the next cycle, a smaller χ^2 is found, increasing the overall precision. The outside loop repeats the whole search process by a given number of cycles, which allow minimizing χ^2 if the available computer

power is large. To gain time and prevent one parameter from remaining less precise than the others, a variable memorizing the digits of each parameter was introduced $\{d(x)\}$. It is used to maintain equilibrium in the search of the optimum, pausing the search of parameters more precise than the others.

3. Plottings:

Finally, after the loop completed all its cycles, the nine determined parameters are saved in a text-file for later use and two plots are generated. The first one is a log-plot of the χ^2 descent speed in function of the number of loop cycles. The second one is a plot of the raw signal and its calibrated version oscillating around the absolute value (B) given in the Preliminary part 1 (see Fig.16).

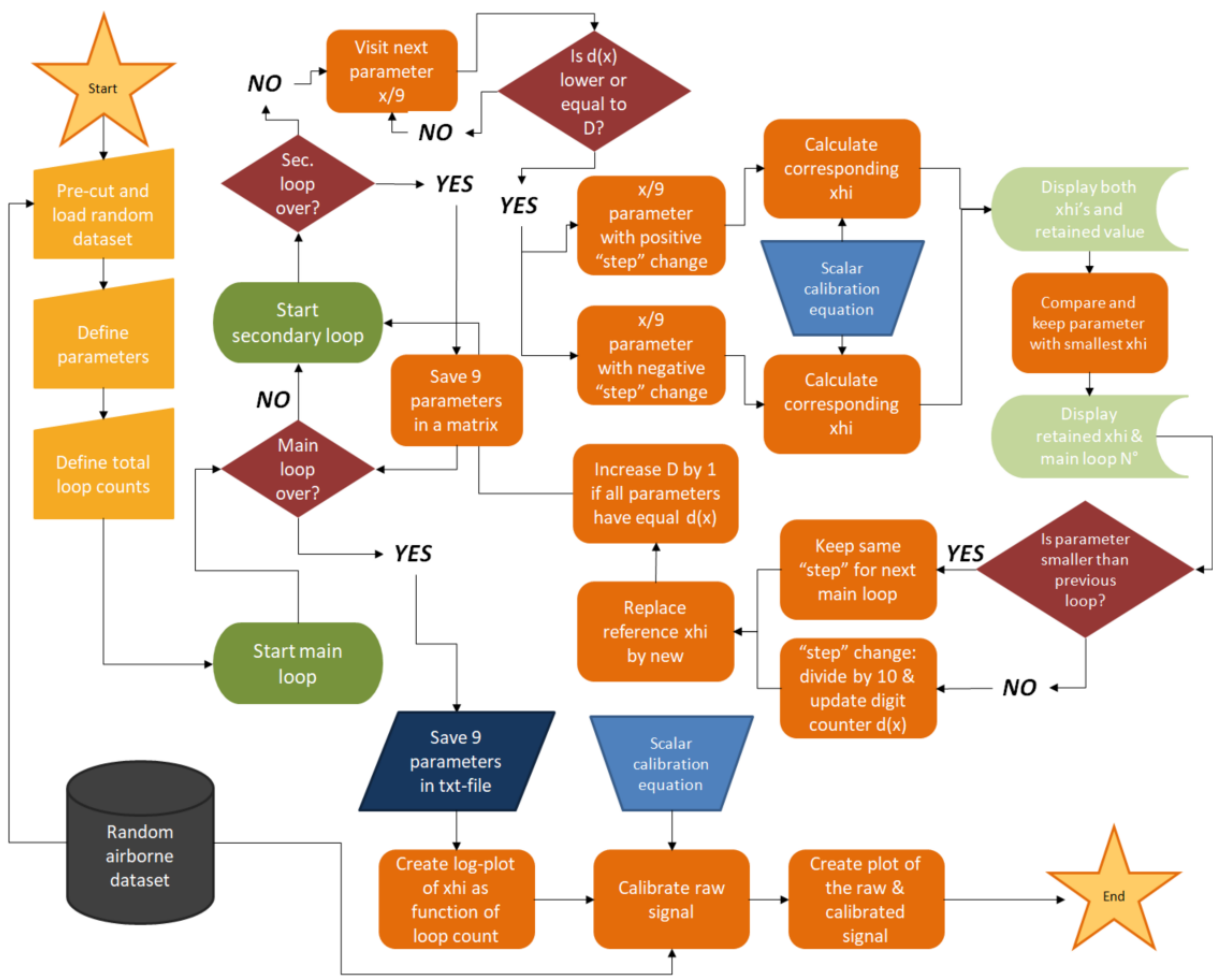


Fig.15 Flow chart of the Matlab script that is used to perform the approximation of the 9 parameters that are used for the scalar calibration.

All this process is done twice in total, one time for sensor 1 and a second time for sensor 2. As mentioned earlier, the resulting nine parameters of both sensors need to be saved to subsequently perform the actual scalar calibration, i.e. equation (3), to the entire missions concerned. Note that if the magnetometer is for some reason unmounted and remounted on the UAV, a new calibration will be

required since it is impossible to remount it the same way as it was, this will impact the effect of the calibration of the following mission. Also, the swap of battery sets requires new calibrations for extra precision.

6.2.4 Example with latest Forel data

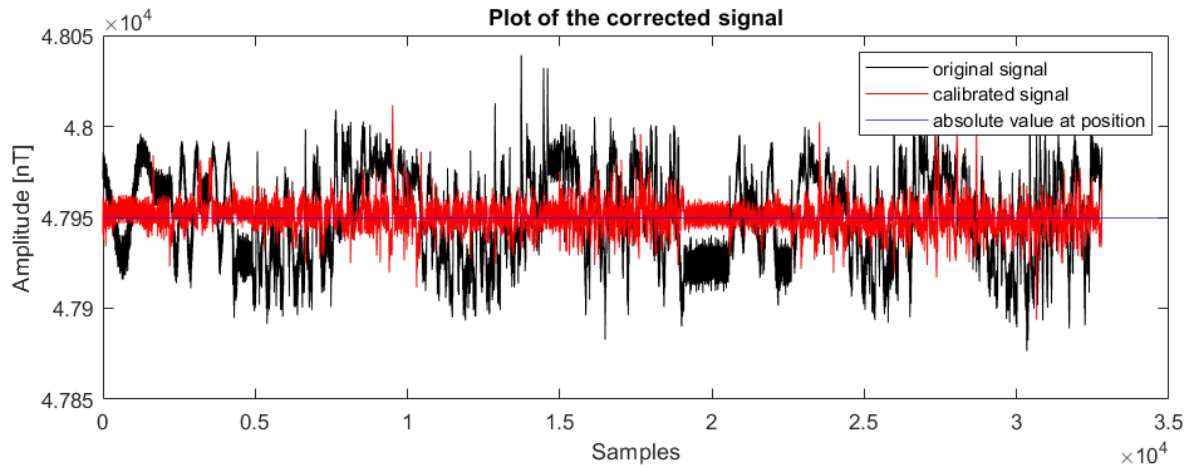
To illustrate the process described above, we will analyze the results of a scalar calibration applied to the latest Forel measurements (Fig.16). The samples, number of loops and standard deviation before and after compensation are listed in Table 10. The scalar calibration was performed with a random dataset produced at the location, at an altitude of 100m above the ground and took around 55min to be completed using a 3.6GHz processor. It generated values for the 9 parameters with a high precision which were then used to compensate the dataset of the missions according to formula (3). Both the raw and compensated signals appear in the graph of Fig.16 as black and red respectively, as well as the numerical values for each of the 9 parameters.

Variable	Value
Samples (x,y and z)	32'801
Loop counts	1200
STD raw signal	37.5038nT
STD corrected signal	7.7641nT

Table 10: List of some variables and results of the scalar calibration performed with a random dataset collected during the latest Forel measurements, 100m above the ground.

The standard deviation (STD) of the compensated signal given in Table 10 appears to be reduced by a factor of nearly five after the calibration was performed. Other papers (Munsch et al., 2007 and Le Maire et al., 2020) show on average between 1-5nT of standard deviation after calibration. One explanation to these even lower standard deviations is the fact that the UAV used was smaller and lighter generating less intense electromagnetic noise.

This compensation is set to reduce the heading error (azimuthal + tilting error described in chapter 5.1 and 5.2). To visualize the improvements, two maps are shown in Fig.17, one having the data with a rather unorthodox correction explained in chapter 5.6 and the other one being magnetically compensated with the above mentioned-technique (chapter 6.2.2).



Vector	Sensitivity	Angle	Offset
X	1.00017100490002	0.00167220000000008	11.6583799999999
Y	1.00025800000008	0.026260999999999	-58.6606999999981
Z	1.00223980000006	-0.04910099999999983	-72.9909999999952

Fig.16 Scalar calibration and compensation results. The two curves represent scalar intensities of the magnetic field of the same acquisition, non-corrected (black line) and corrected (red line).

The first obvious difference in Fig.17 is that the majority of “anomalies” that were present in A) disappeared in B). They were all mostly due to the heading error. The geomagnetic image was also improved where the UAV performed the U-turns, rendering the edges of both latest missions qualitatively useful. The red circles indicate the strongest anomalies to provide landmarks for better comparison. Many more points are common to both magnetic maps.

It is visible in B) that two areas (rectangles) appear more yellow overall than the rest; they are indicated by the yellow brackets. These sections were flown with the set of 120Wh batteries, whereas the rest with the 99Wh battery sets. Since only one random dataset was used to calibrate all the missions, and since the battery pack present in the drone at the time of the acquisition of such dataset was the 99Wh battery pack, the calibration resulted to be less adequate for both missions flown with the different sized batteries. Even so, the results after scalar calibration proved to be of spectacular improvement. See in the Appendix (9.4-9.6) the final anomaly and gradient maps along with the orthophoto.

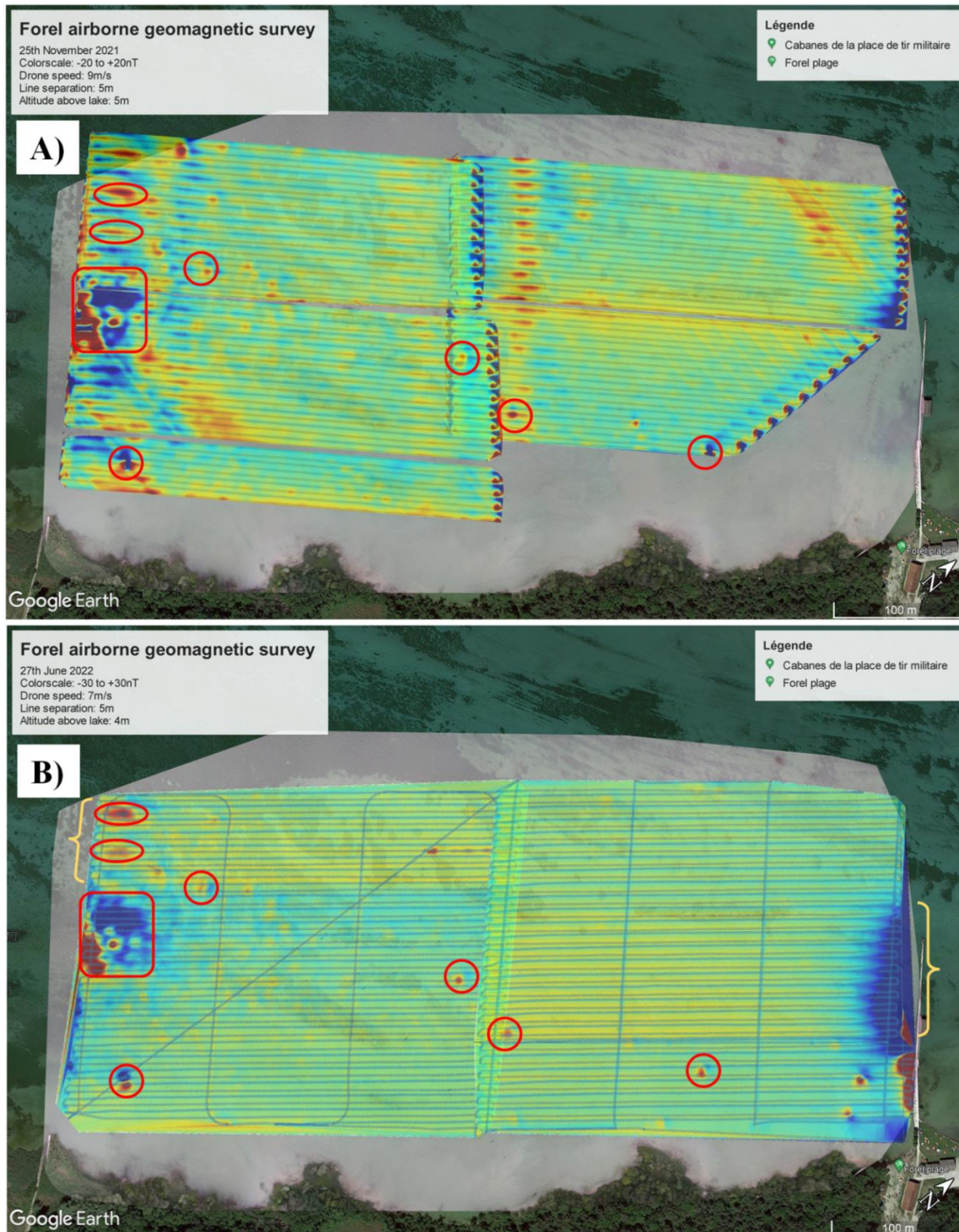


Fig.17 Geomagnetic maps from the Forel military bombing range displayed on top of an orthophoto taken the same day; A) data acquired in September 2021 and processed according to steps described in chapter 4.5 with azimuthal error correction (without magnetic compensation) and B) data acquired in June 2022 also processed with steps from chapter 4.5 but with magnetic compensation (described in chapter 6.2.2), data covering a larger area than A and divided in two large patches (Northern & Southern, with overlap). The areas circled in red represent the most intense anomalies visible on both sides. Yellow brackets indicate portions surveyed with 120Wh batteries (otherwise 99Wh).

6.2.5 Gradient interpretation

One method to highlight low amplitude UXO-related signals is to use the gradient of the signal. The gradient corresponds to the first derivative of a function and is easily calculated with the same software used in the processing part, i.e. Matlab. Since it is calculated along a curve, it is 1-dimensional and does not contain information on the perpendicular (2D) or vertical axis (3D). After performing the gradient calculation and to enhance the readability of the anomaly maps, interpolation will be used to cover the entire 2D map.

The purpose is illustrated in a synthetic example (Fig.18) assuming a geomagnetic signal that was recorded with an airborne sensor above a magnetic object buried just below the surface (A). Note, for simplicity the Earth's magnetic field was omitted. The first encounter with the negative magnetic field of the object produces a negative anomaly preceded by a positive one (B) due to the positive field at the other end of the object. The synthetic anomaly has a scalar intensity of +/- 100.

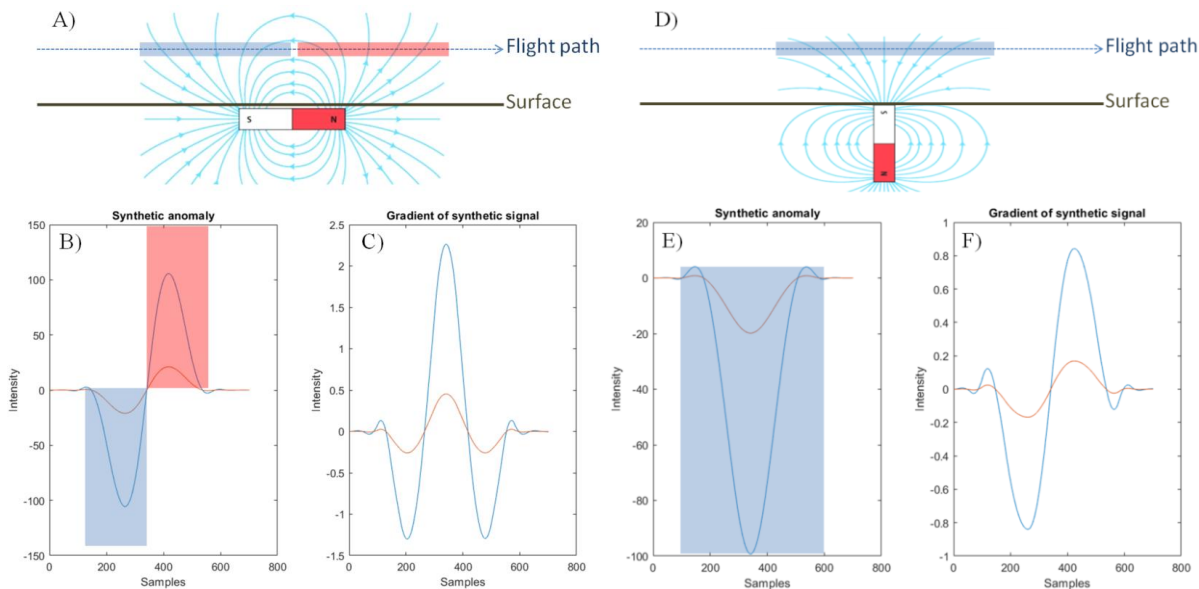


Fig.18 Synthetic experiment where A data are acquired above a magnetic object with both field components (+ and -) emerging above the surface and plotted in B along with their corresponding gradient in C. The blue curve represents an anomaly of +/-100nT and the orange curve of +/-20nT, with a peak gradient at 2.3 and 0.5 respectively. It is important to see that the synthetic signal is symmetrical with both peaks off-centered whereas the gradient's peak is centered in the middle of the anomaly.

A second synthetic experiment is shown in D where only the negative component of the magnetic field emerges above the surface, corresponding to a signal E along with the gradient of the signals F whose peaks are not on the center of the object this time.

The corresponding gradient of the above described synthetic anomaly is shown on Fig.18 C and has a much lower amplitudes than the anomaly itself, because the gradient describes the variations of

intensity with time (here, with the increasing amount of samples). One can see that the shape of the gradient is symmetrical along the x-axis, where the peak is highest; this corresponds to the location of the magnetic object. It appears at first, that thanks to this feature, the visual localization of UXO will be easier on 2D maps but if we look at the sketch D), the signal has only a negative component due to the orientation of the magnetic object. This corresponds to a U-shaped signal (E) which in turn has an S-shaped gradient (F) that misleads the exact position of the object by having 2 maxima (one peak and one trough). For consistency, the anomaly was set to -100nT (blue curve) and -20nT (orange curve) and we can see that the gradient already differs for both having an amplitude more than twice as small as the previous example.

As mentioned above, it is the variations of intensity in the synthetic anomaly that produce a signal in the gradient; the steeper the variations of the signal, the steeper the gradient. Slow and gradual variations will have a gradient close to 0 and therefore won't appear visible in the color map. The gradient method is in other words, a good way to highlight steep signal changes, and thus anomalies.

In the following, we will compare an anomaly map with its gradient counterpart. As for the anomaly map, a good (empirical) compromise must be found with regards to the minimum and maximum values of the color scale, in order to visualize as many anomalies as possible without highlighting noise. It was found that ± 2 nT/sample was a good compromise.

On Fig.19 we can observe two maps corresponding to the Northern part of the latest Forel mission (cf. Fig.17 B). We can see that the second map (II), which is the gradient map of the signal displayed in (I), is smoother and easier to interpret. There are in fact no more amplitude differences between the come and go as for the signal map. The strongest anomalies, circled in red, appear now clearly recognizable. Some anomalies, circled in blue, appear in the gradient map whereas they are hardly observable in the anomaly map. To be sure that the blue circled anomalies are in fact anomalies and not noise, we need to perform an analysis of the signal of each track separately. This process is shown in the next part.

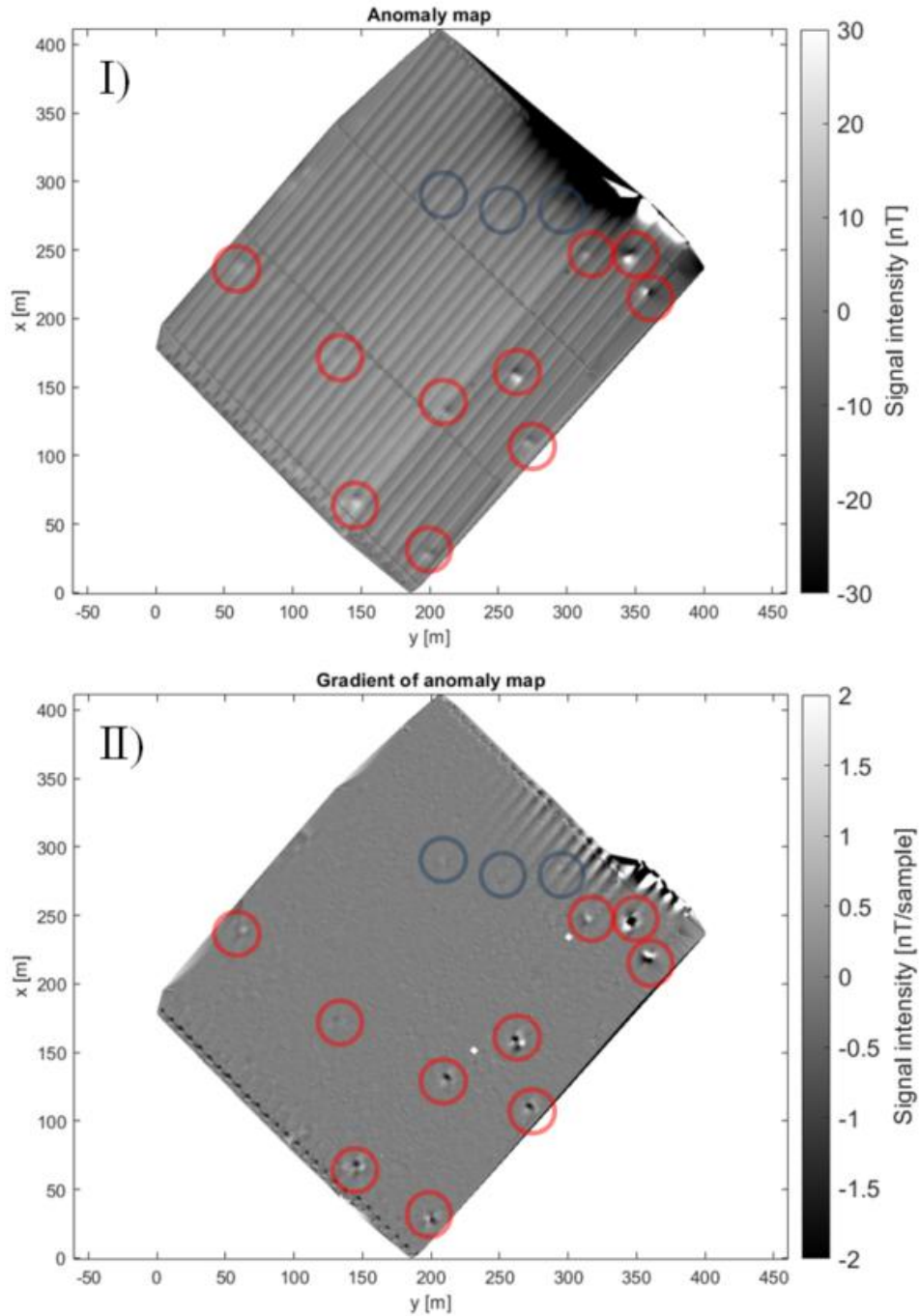


Fig.19 Maps representing the same area (Forel, northern survey) with identical data treatment as Fig.18, where I consists of the signal and II its gradient equivalent in [nT/sample], where “sample” represents here one 10th of the original sampling rate due to the decimation. Circled in red are visible anomalies in both maps. Circled in blue are anomalies only identified on the gradient map, transferred to the anomaly map; they aren’t always as clearly visible as in II. Note that in I the flight lines are not plotted but appear visible due to slightly different intensities on each come and go of the UAV. The black area in the North-Eastern part of the map corresponds to a concrete pier.

To understand and see if the anomalies appearing in Fig.19 have a signature close to those described in Fig.18, it is helpful to analyze the data along the profile corresponding to the red track in Fig.20 C).

The signal plotted in A contains 3 anomalies (indicated with the red arrows) with decreasing amplitude from arrow n°1 to 3. They are all mostly positive anomalies, except number 3 because it has a steep negative gradient change that makes it hard to interpret. Since this is happening right before the U-turn it is probably being influenced by the turning maneuver, so it will be disregarded as well as the first 100 samples before anomaly 1. Anomalies 1 and 2 have a gradient signature that is similar to those discussed above and are certainly of artifact origin, and if not, of natural cause such as ferromagnetic boulders (glacial erratics).

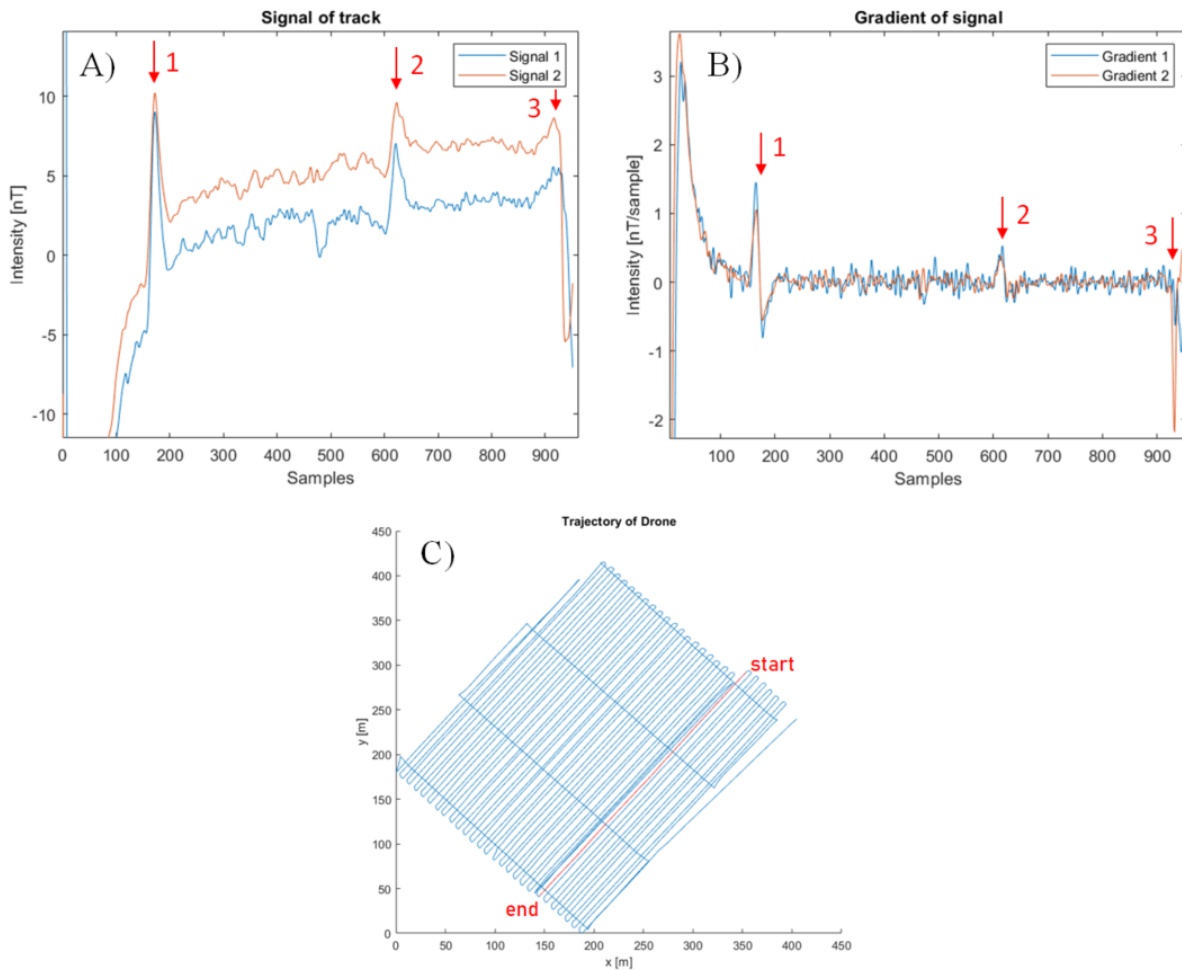


Fig.20 Plot of the selected red track in C from the Forel northern mission with the corresponding signal plotted in A along with the respective gradient in B, from both sensor 1 (in blue) and sensor 2 (in orange).

This in-depth analysis should be repeated for the entire anomaly map to identify with more clarity and certainty whether the anomalies have a recognizable signature or not. Subsequently, on-site analysis of the identified location would be required in order to inspect the highlighted locations and confirm whether or not the anomalies are due to UXOs or any other cause such as ferromagnetic boulders, buoys and scrap metal or similar.

6.3 Topography positioning corrections

In the following, we will take a closer look to what can be done in order to improve the accuracy of the positioning of the aircraft and the measurements from errors described in Table 7 (cf. chapter 5.3). We will separate the analysis in 4 parts: (1) the 99 waypoints limit, (2) the digital terrain model related issues, (3) the GPS of the UAV and (4) the GPS of the magnetometer.

(1) As mentioned in chapter 4.2 and 5.3, the M600 was designedly limited to a maximum use of 99 waypoints. We have seen that this greatly limited the size of missions especially if the terrain was rugged, with an AGL tolerance of 1m. One trivial solution, but at the cost of precision, would be to increase such tolerance. The mission planner would then recalculate the mission with fewer waypoints. This would allow larger missions to be flown at once. If the terrain is very rugged, the flying speed should be decreased such that the UAV has enough time to adjust its altitude. However, there is another solution to this problem that doesn't have to make compromises: swapping the flight controller (FC) of the M600 with an aftermarket one, running on an open source firmware such as android or arduino. This would allow a close to infinite number of waypoints to be stored (depending on the memory size) but at the cost of the reliability of the triple redundant A3 module from DJI. An open source firmware would also facilitate the integration of third party sensors such as RTK-antennas or laser-to ground positioning devices that are provided at lesser costs by other manufacturers. Doing so would probably take a day of lab work and around maximum a few hundred dollars for the new FC. However, this would also break the warranty provided by the constructor, so the benefits should always be carefully weighed against the costs.

(2) The default digital terrain model (DTM) of the mission planner is the SRTM-4 (cf. chapter 5.3) and is, as we have seen, not reliable for very close to surface surveys. Instead, there is the option to load DTMs from other sources, such as swisstopo⁸ or others for foreign countries. This approach was successfully implemented in the latest Forel surveys removing irregularities over the lake that were present in the initial Forel measurements. Another idea to be even more precise would be to create an in situ DTM with aerial photogrammetry. The M600 is capable of such thing, but any other drone that has a decent camera and positioning system can perform usable photogrammetry files. This would have the advantage of yielding highly accurate DTMs even in remote places at the cost of a pre-survey flight. Using a second drone (lighter and cheaper) to generate an in situ DTM would save the batteries of the M600 for the magnetic survey right after. This system would have a cost of a regular drone (ca. 1000\$) and add perhaps around 1h of labor to the fieldwork project. Nevertheless, this approach wasn't tested yet.

(3) With respect to the positioning of the M600, the triple redundant GPS system, the only way to increase its accuracy would be to swap it with an RTK system which is up to millimeters accurate. The

⁸ Swisstopo is the Swiss Federal Office of Topography

disadvantage of such system is that it requires a connection with a fixed base station that has to be in a range of <10km; this is rarely the case in remote places. If only altitude accuracy is of importance, then the use of a laser positioning system should be the device of choice, requiring no such connection. Both systems have a cost nowadays of several thousand dollars.

(4) The magnetometer has its own GPS but for most of the surveys carried out until today its accuracy was in the order of 1-3m (cf. Table 6, chapter 5.3). In addition to that, the device is placed below the M600 and has only one single GPS receiver. Between the M600 and the MagDrone, the M600 has definitely a better GPS reception and probably a more accurate signal too. Hence, we could use the GPS data from the log files from the flight controller of the M600 and assign it to the magnetic dataset to increase to precision of the measurements. This solution would have no financial cost but would require an effective method of downloading the heavy log files and finding the identical GPS time to assign the correct coordinates to the right measurement.

All the above listed possibilities of improvement for topographic corrections come at an increased financial cost and processing time. In the following we will review and compare their cost and benefits with respect to one another.

Topography positioning solutions - costs and benefits				
N°	Problem	Solution	Cost	Benefit
(1)	99 waypoints limit	FC swap	<200\$ + 1d	Up to meters increased accuracy
(2)	DTM SRTM-4 accuracy	Load DTM from other sources	<100\$ + <1h each time	Increased accuracy
		Create own DTM with photogrammetry	<1000\$ one time + 1h each time	Increased accuracy everywhere
(3)	M600 GPS accuracy	RTK integration	<3000\$ one time + <1d one time	Increased accuracy where RTK signal available
		Laser to ground positioning	<3000\$ one time + <1d one time	Altimetry cm accurate
(4)	MagDrone GPS accuracy	Use log data from M600	0\$ + <1h each time	Up to meters increased accuracy

Table 11: Recap table of the topography positioning error sources and their solutions with their respective costs and benefits based on a rough estimation.

As table 11 indicates, the solutions to increase the positioning accuracy have varying costs and benefits. For instance, the cheapest solution which would already yield an increase in accuracy of up to meters is the use of the GPS log data from the M600 instead of the MagDrone itself. The one-time challenge would be to find an effective way of downloading these (heavy) files and retrieving only the segment corresponding to the measurements pasting it to the magnetic measurements without losing time in between.

I would personally recommend swapping the FC of the M600. Although the original triple redundant system is extremely reliable, other manufacturers match DJI professional quality in terms of robustness offering, on top of that, an open source firmware. In addition, if it is beneficial for the accuracy of the survey, the researchers should load DTMs from swisstopo (or any other source) if it is more precise than the SRTM-4. Also, if the budget allows it, a laser to ground positioning system would be of relevance, especially for close to ground surveys such as for UXO or archeological detection. Finally, in the case of close to ground surveys, I would also recommend finding a way to make use of the GPS log data from the UAV instead of using the default GPS data from the MagDrone, because differences of $\pm 1\text{m}$ will matter for the positioning of anomalies. Beware that swapping the FC could also mean substituting the triple GPS system because DJI devices are not necessarily compatible with third party devices.

6.4 Color coding for qualitative interpretation

The color scaling choice for geomagnetic maps was shown in chapter 5.5 to be a relevant factor for an accurate qualitative interpretation. In fact, some color scales will either highlight or underemphasize anomalies/artifacts and either facilitate or complicate the interpretation of such items. In the following we will proceed with a deep comparison and analysis of various color scales in order to identify suitable color scales for (1) archeological/UXO detection and (2) geological structures identification. As a matter of fact, both survey types differ immensely in size and altitude; the first (1) being usually very close ($<10\text{m}$) to the surface with very dense survey lines ($<10\text{m}$) and lateral sizes never exceeding a few hundred meters in length (allowing the interpreter to be able to still identify artifacts on A4 printed maps). The second type (2) is usually carried out at higher altitudes (10-100m) above ground over larger areas up to several kilometers long. The type of anomalies expected in such case is much larger and intense in terms of signal amplitude than the more local type (1) survey.

Concerning (1) archeological/UXO detection, a mission from the Forel site was chosen. For this type of survey, large to small dipole anomalies are of interest as well as anomalous areas with large magnetic field variations that are indicative for concentrations of metallic objects. Sensitive scales with a large spectrum of colors might help locate these but might also highlight natural transitions which are of no interest to us in this case.

The color scale “hsv” on Fig.21 has 3 strong color transitions, the yellow, the turquoise and the pink zones. Values within the range of these transitions will appear eye-catching. Another issue with this color scale is the fact that both extremes are in the red range. The “jet” color scale is somewhat smoother but there are still two transitions appearing with strong contrast, they are in the turquoise and yellow region again, producing similar undesired phenomena to the eye of the interpreter. The color

scale “turbo” was designed in a way to remove these turquoise and yellow strong transitions. It appears smoother than the “jet” one and might already be a convenient solution.

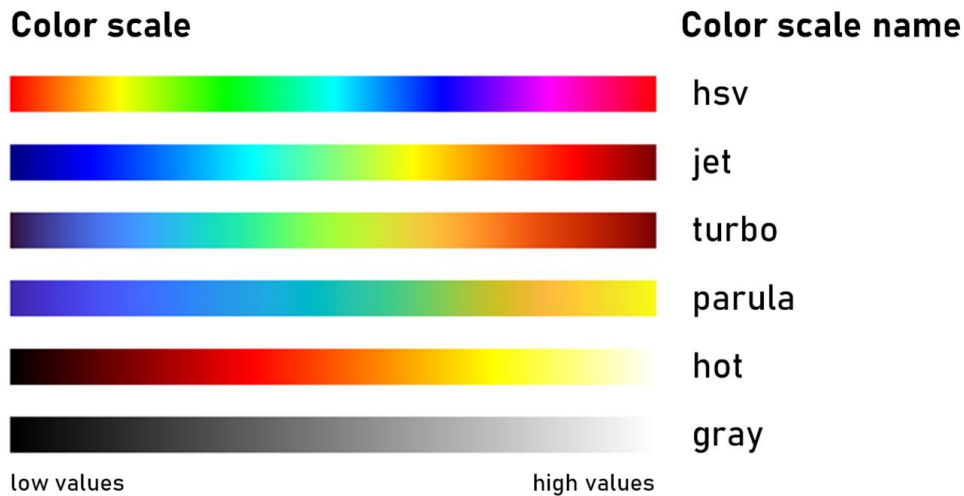


Fig.21 List of 6 color scales with their respective names (Matlab) that are tested and compared for archeological/UXO detection.

The “parula” color scale (cf. Fig.21) is different in the way that the high values end with orange to yellow colors and not red anymore. The eye-catching transition in this case appears in the green-yellowish zone at around two thirds of the color scale. The “hot” color scale has also the high values end in the bright yellow range but low values starting in black-dark red. High and low values tend to appear diminished as the contrast is reduced. Finally, the “gray” scale, with black and white for low and high values; this scale was already presented in chapter 5.5 and is typically used by archeologists.

In the following, the list of color scales in Fig.21 is applied to the same dataset (Forel, mission 4). This dataset underwent the processing steps 0-8 (cf. chapter 4.5) and differ for every figure only in the 9th step which is the plotting scheme step.

As expected, the “hsv” (Fig.19 A) is one of the worst in matters of over-emphasizing remaining heading errors for reasons mentioned above. The “jet” (B) and “turbo” (C) show similar trends but differ in the display of the 0, for which “turbo” tends to be more consistent throughout the entire mission. However, it has strong color transitions near the 0 that emphasize the residual heading error. Plot B tends to mix bluish and greenish colors for data oscillating near 0. Plot D is also rather smooth near the 0 but lacks a bit the contrasts of the other color scale to quickly identify low intensity anomalies. Plot E and F look very similar with only a change in color. It appears that the “hot” color scale has more contrast than the “gray” scale. In conclusion, the “parula” and “hot” are the preferred color scales for (1) archeological/UXO detection.

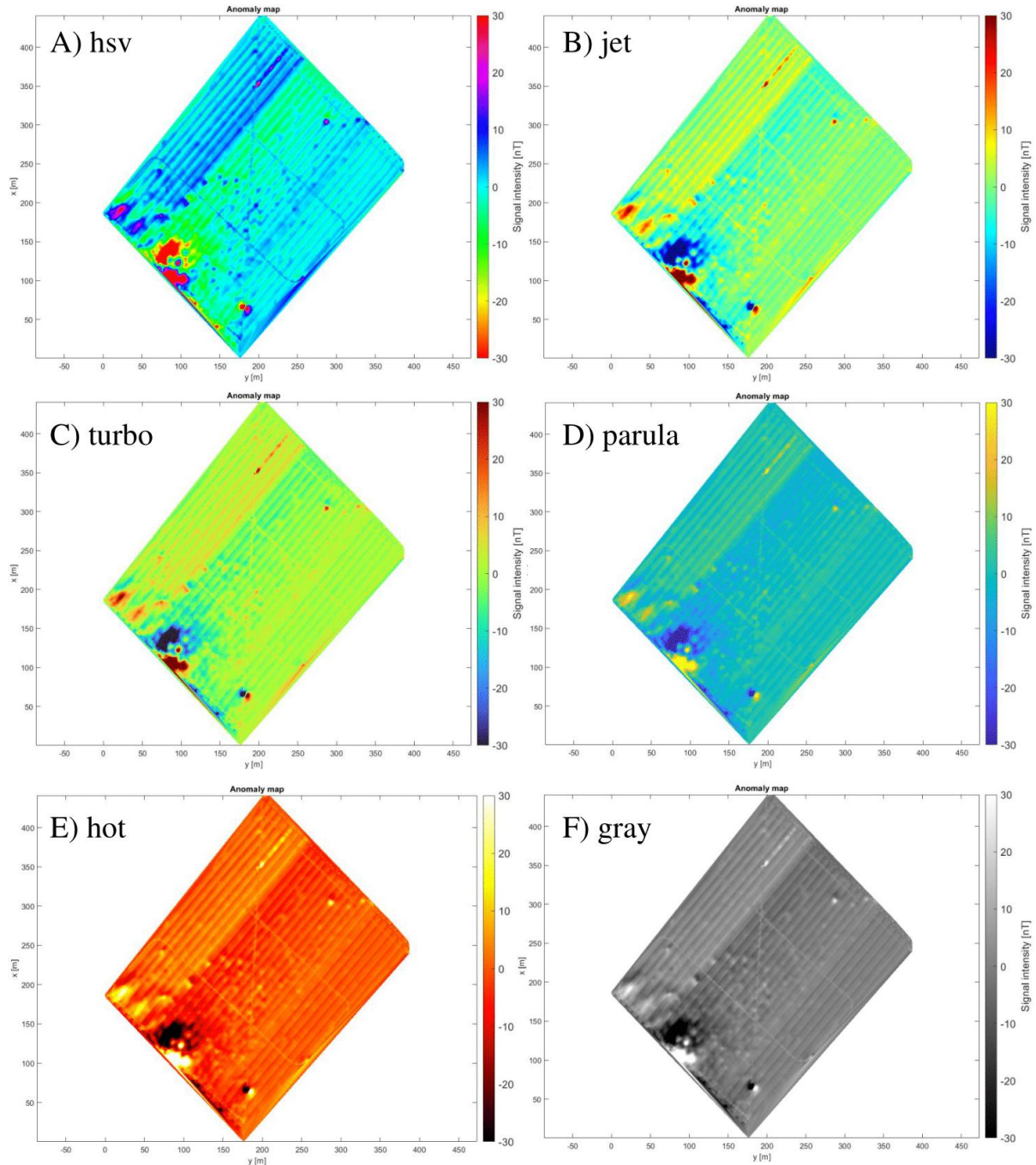


Fig.22 Six plots of the dataset from Forel (mission 4) with exclusively the color scale (see Fig.21) varying and processed according to chapter 4.5 steps 1-8 (9th varying). In A) the color scale “hsv” is applied; B) color scale “jet”, C) color scale “turbo”, D) color scale “parula”, E) color scale “hot” and F) color scale “gray”.

Concerning (2) geological structure identification, a dataset from the Mongolia project was used. In this case we are concerned about structures in the order of several decameters. Trying to identify smaller features would be impossible because of the altitude at which the survey was carried out, here 45m above ground.

As discussed above, the “hsv” color scale doesn’t suit magnetic maps because of the overemphasis on transitions that do not exist. This is the disadvantage of so-called non-continuous color scales. The “gray” scale is also not adequate because of its already widespread use in the archeological field for highlighting artifacts. We are left with only 4 color scales to compare and analyze, named “jet”, “turbo”, “parula” and “hot” (cf. Fig.23).

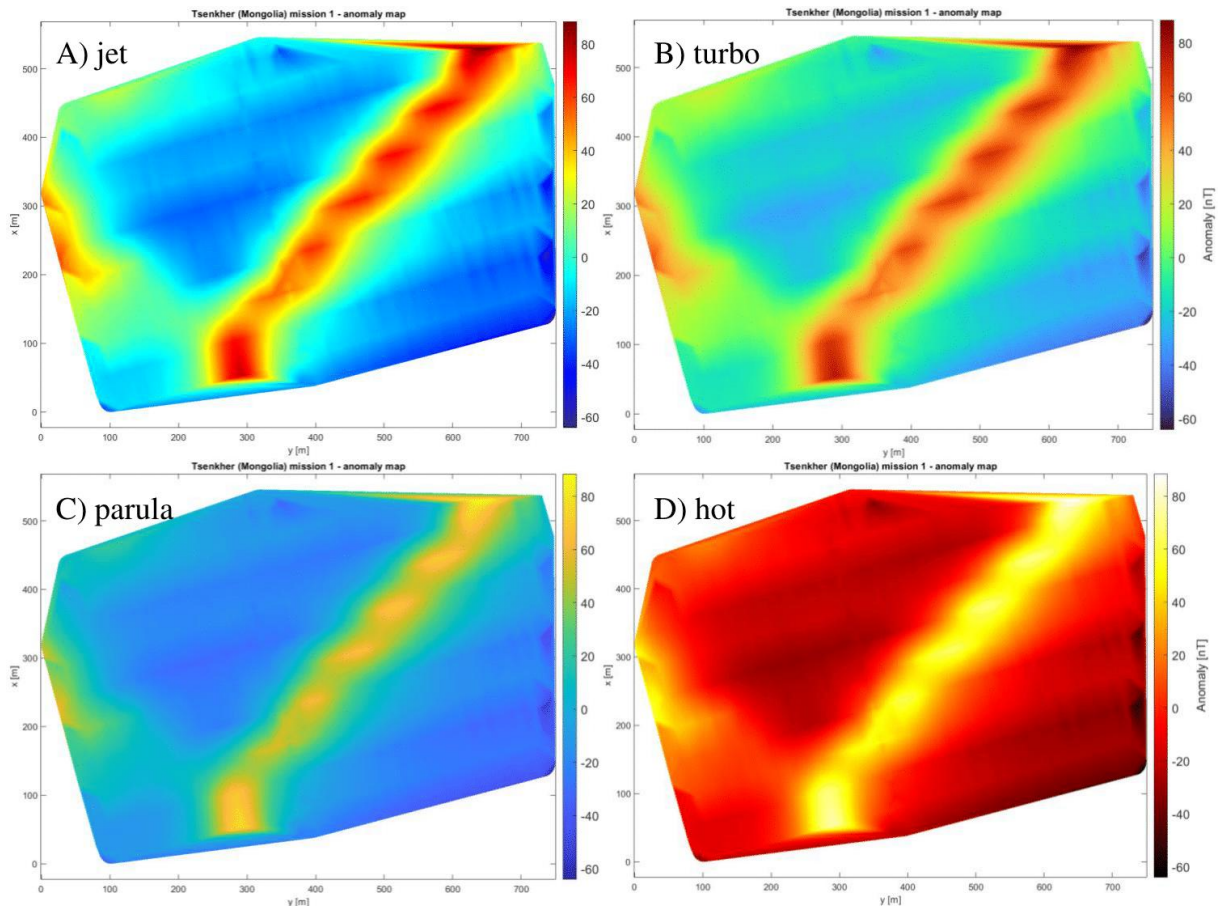


Fig.23 Four plots of the dataset from the Mongolia project with exclusively the color scale (see Fig.21) varying, processed according to chapter 4.5 steps 1-8 (9th varying). In A) the color scale “jet” is applied; B) color scale “turbo” is applied, C) color scale “parula” is applied and D) color scale “hot” is applied. The anomaly was interpreted by Aubert (2019) to be caused by a basaltic dyke which occur regularly in this region.

Plot A and B are again very similar, but the “turbo” colors scale seems to be smoother around the 0 value. This affects in a visible manner the edges of the basaltic dyke, which seem to be independent sections themselves in A rather than part a whole as in B. The “parula” color scale is here too, lacking the contrast both A and B have, but at the advantage of decreasing the anomaly that is present between the Eastern part and the basaltic dyke. Finally, plot D is a good compromise between contrast and the absence of highlighting artificial transitions.

7. Conclusion

We have seen that UAV's can be used not only for photography or as a hobby device, but also for scientific research with applications that were until recently preferred by hand or helicopter. The use of an UAV proved to be the only available option for surveying a very shallow lake area quickly and providing reliable data.

This data was the substrate of this research, where the final goal was to improve the quality of airborne geomagnetic maps for better qualitative interpretation. This goal was achieved after a thorough description and understanding of the implications and complications arising in autonomous airborne surveys by UAV.

The scalar calibration scheme (chapter 6.2.2), although already existing for satellite calibration and even UAV's in the case of private companies, was used as basis to create an algorithm which was not disclosed publically and comprehensibly until today. The effectiveness of such algorithm was successfully demonstrated using real data and comparing it with alternate one.

Moreover, additional corrections and upgrades for close to ground surveys, such as using better GPS data from the UAV rather than from the magnetometer, as well as using higher quality digital terrain models or the optional use of laser or RTK positioning systems among other could keep refining the precision of today's magnetic maps. Additionally, the non-obvious choice of clever color scales yielded different solutions in the case of surveying at low or high altitude.

This research does not pretend to address all the problems in the sphere of airborne surveys, but is another small step proposing solutions in particular for the equipment that the ETH Zürich possesses.

The future for airborne surveys, whether for magnetism, EM or even georadar among others, is still full of possibilities and challenges, which in the end will present opportunities to further study remote or inaccessible areas by foot or other vehicles. Scientists that are often in the field not using these tools should probably start learning to make use of them, because they will, on many occasions, simplify their lives.

8. References

- Aubert, F. (2019), Development of an airborne geomagnetic mapping system, ETH Zürich
- Armasuisse, organization + factsheet, accessed 08 March 2022: <<https://www.ar.admin.ch/en/ueber-armasuisse/organisation.html#ui-collapse-958>>
- Crameri, F., Shephard, G.E. & Heron, P.J. The misuse of colour in science communication. *Nat Commun* 11, 5444 (2020). <<https://doi.org/10.1038/s41467-020-19160-7>>
- Geomagnetic observatories catalog, accessed 07 March 2022:
<<https://dataservices.gfz-potsdam.de/intermagnet/showshort.php?id=escidoc:3314891>>
- Le Maire, P., Bertrand, L., Munsch, M., Diraison, M. and Géraud, Y. (2020), Aerial magnetic mapping with an unmanned aerial vehicle and a fluxgate magnetometer: a new method for rapid mapping and upscaling from the field to regional scale. *Geophysical Prospecting*, 68:2307-2319. <<https://doi.org/10.1111/1365-2478.12991>>
- Macharet, D.G.; Perez-Imaz, H.I.; Rezeck, P.A.; Potje, G.A.; Benyosef, L.C.; Wiermann, A.; Freitas, G.M.; Garcia, L.G.; Campos, M.F (2016) Autonomous Aeromagnetic Surveys Using a Fluxgate Magnetometer. *Sensors*. 16. DOI: 10.3390/s16122169
- Magnetic declination, inclination and field strength based on the World Magnetic Model WMM2020 (for any location on Earth), accessed 15 March 2022:
<<https://www.magnetic-declination.com>>
- Mathé, V., Lévêque, F., and Druez, M. (2009), “What interest to use caesium magnetometer instead of fluxgate gradiometer?”, *ArcheoSciences*, 33 (suppl.), 325-327
<<http://journals.openedition.org/archeosciences/1781>>
- Munsch, M., Boulanger, D., Ulrich, P., Bouiflane, M. (2007), Magnetic mapping for the detection and characterization of UXO: Use of multi-sensor fluxgate 3-axis magnetometers and methods of interpretation, *Journal of Applied Geophysics*, Volume 61, Issues 3–4, 2007, Pages 168-183, ISSN 0926-9851. <<https://doi.org/10.1016/j.jappgeo.2006.06.004>>
- Mukul, M., Srivastava, V., Jade, S., & Mukul, M. (2017), Uncertainties in the Shuttle Radar Topography Mission (SRTM) Heights: Insights from the Indian Himalaya and Peninsula. *Scientific reports*, 7, 41672. <<https://doi.org/10.1038/srep41672>>
- Nabighian, M. N., V. J. S. Grauch, R. O. Hansen, T. R. LaFehr, Y. Li, J. W. Peirce, J. D. Phillips, and M. E. Ruder (2005), The historical development of the magnetic method in exploration: *Geophysics*, 70, no. 6, 33ND–61ND. <<http://dx.doi.org/10.1190/1.2133784>>

- Olsen, N., Tøffner-Clausen, L., Sabaka, T.J., Brauer, P., Merayo, J.M., Jørgensen, J.L. et al., (2003) Calibration of the Ørsted vector magnetometer. *Earth Planets Space*, 55, 11–18
- Parshin, A. V., Morozov, V. A., Blinov, A. V., Kosterev, A. N. & Budyak, A. E., (2018) Low-altitude geophysical magnetic prospecting based on multirotor UAV as a promising replacement for traditional ground survey, *Geo-spatial Information Science*, 21:1, 67-74, DOI: 10.1080/10095020.2017.1420508
- Primdhal, F. (1979), The fluxgate magnetometer. *J. Phys., E Sci. Instrum.* 12, 241–253
- FOCA, Regulations and general questions relating to drones, Federal Office of Civil Aviation (FOCA), accessed 09 March 2022: <<https://www.bazl.admin.ch/bazl/en/home/good-to-know/drones-and-aircraft-models/allgemeine-fragen-zu-drohnen.html>>
- SRTM v4.1 digital elevation database, accessed 05 April 2022: <<https://cgiarcsi.community/data/srtm-90m-digital-elevation-database-v4-1/>>

9. Appendix

9.1 Matlab script to find parameters for the scalar calibration of one sensor

```
% Scalar Calibration By Franco Aubert (2022)  
% Based on equations by Olsen et al. (2003)
```

Init

```
clear all  
close all  
clc  
  
B = 47950; %abs mag intensity of location (Forel=47950nT as per WMM2020)  
  
% Select dataset for calibration (one single trace)  
load ('C:\Users\auber\OneDrive\Documents\Master\Msc Thesis\Data & Scripts\Forel June  
22\MagData\Calibration\mat\20220627_133138_MD-R3_#0027_99Wh.mat');  
  
%Choose which sensor to perform calibration on:  
F_raw = [MagData.Drone.B.B1x MagData.Drone.B.B1y MagData.Drone.B.B1z]';  
%F_raw = [MagData.Drone.B.B2x MagData.Drone.B.B2y MagData.Drone.B.B2z]';  
  
dec = 10; %decimation factor for faster processing, use 1 for no decimation  
F(1,:) = decimate(F_raw(1,:),dec);  
F(2,:) = decimate(F_raw(2,:),dec);  
F(3,:) = decimate(F_raw(3,:),dec);  
  
% Manual input of parameters:  
s1 = 1.1;  
s2 = 1.1;  
s3 = 1.1;  
u1 = 0.001;  
u2 = 0.001;  
u3 = 0.001;  
o1 = 0.00;  
o2 = 0.00;  
o3 = 0.00;  
  
% Vector to store the 9 parameters  
a = [s1; s2; s3; u1; u2; u3; o1; o2; o3];  
  
% Generate first xhi with (random) values  
[S,P,O] = P9(a); %function to generate matrices with parameters  
xhi1 = f_xhi(B,F,S,P,O); %function to generate misfit with inv of matrices
```

Auxiliary variables for loop

```
a2 = a;  
a3 = a;  
xhi2 = xhi1;  
xhi3 = xhi1;  
step1 = 0.01;
```

```

step2 = 0.01;
step3 = 0.01;
step4 = 0.01;
step5 = 0.01;
step6 = 0.01;
step7 = 10;
step8 = 10;
step9 = 10;
M_9p = {[ ]; [ ]; [ ]};
d = zeros(9,1); %vector to store digits of each parameter
d(1) = numel(num2str(s1));
d(2) = numel(num2str(s2));
d(3) = numel(num2str(s3));
d(4) = numel(num2str(u1));
d(5) = numel(num2str(u2));
d(6) = numel(num2str(u3));
d(7) = numel(num2str(o1))+3;
d(8) = numel(num2str(o2))+3;
d(9) = numel(num2str(o3))+3;
D = max(d);

```

Loop for parameter reduction

```

loop =200; %number of loop counts (to modify)

for l = 1:loop
    % loop inside for each of the 9 parameter for a individual reduction
    for z = 1:9

        %Parameter s1
        if z == 1 && d(1) <= D
            % Generate xhi with small parameter difference -
            a2(z) = a2(z)-step1;
            [S2,P2,O2] = P9(a2); xhi2 = f_xhi(B,F,S2,P2,O2);
            disp(['s1 xhi - : ',num2str(xhi2)])

            % Generate xhi with small parameter difference +
            a3(z) = a3(z)+step1;
            [S3,P3,O3] = P9(a3); xhi3 = f_xhi(B,F,S3,P3,O3);
            disp(['s1 xhi + : ',num2str(xhi3)])

            if xhi2 < xhi1
                S = S2; P = P2; O = O2;
                diff = xhi1-xhi2;
                a3 = a2;
            elseif xhi3 < xhi1
                S = S3; P = P3; O = O3;
                diff = xhi1-xhi3;
                a2 = a3;
            else %undo the step that was done and reduce step by factor 10
                a2(z) = a2(z)+step1;
                a3(z) = a3(z)-step1;
                step1 = step1/10;
                d(1) = d(1)+1; %Update amount of digits of parameter
            end
        end
        %Generate xhi with correct decreasing parameters
    end
end

```

```

xhi1 = f_xhi(B,F,S,P,0);

%Parameter s2
elseif z == 2 && d(2) <= D
    % Generate xhi with small parameter difference -
    a2(z) = a2(z)-step2;
    [S2,P2,O2] = P9(a2); xhi2 = f_xhi(B,F,S2,P2,O2);
    disp(['s2 xhi - : ',num2str(xhi2)])

    % Generate xhi with small parameter difference +
    a3(z) = a3(z)+step2;
    [S3,P3,O3] = P9(a3); xhi3 = f_xhi(B,F,S3,P3,O3);
    disp(['s2 xhi + : ',num2str(xhi3)])

    if xhi2 < xhi1
        S = S2; P = P2; O = O2;
        diff = xhi1-xhi2;
        a3 = a2;
    elseif xhi3 < xhi1
        S = S3; P = P3; O = O3;
        diff = xhi1-xhi3;
        a2 = a3;
    else
        a2(z) = a2(z)+step2;
        a3(z) = a3(z)-step2;
        step2 = step2/10;
        d(2) = d(2)+1; %Update amount of digits of parameter
    end
    %Generate xhi with correct decreasing parameters
    xhi1 = f_xhi(B,F,S,P,0);

%Parameter s3
elseif z == 3 && d(3) <= D
    % Generate xhi with small parameter difference -
    a2(z) = a2(z)-step3;
    [S2,P2,O2] = P9(a2); xhi2 = f_xhi(B,F,S2,P2,O2);
    disp(['s3 xhi - : ',num2str(xhi2)])

    % Generate xhi with small parameter difference +
    a3(z) = a3(z)+step3;
    [S3,P3,O3] = P9(a3); xhi3 = f_xhi(B,F,S3,P3,O3);
    disp(['s3 xhi + : ',num2str(xhi3)])

    if xhi2 < xhi1
        S = S2; P = P2; O = O2;
        diff = xhi1-xhi2;
        a3 = a2;
    elseif xhi3 < xhi1
        S = S3; P = P3; O = O3;
        diff = xhi1-xhi3;
        a2 = a3;
    else
        a2(z) = a2(z)+step3;
        a3(z) = a3(z)-step3;
        step3 = step3/10;

```

```

        d(3) = d(3)+1; %Update amount of digits of parameter
    end
    %Generate xhi with correct decreasing parameters
    xhi1 = f_xhi(B,F,S,P,O);

%Parameter u1
elseif z == 4 && d(4) <= D
    % Generate xhi with small parameter difference -
    a2(z) = a2(z)-step4;
    [S2,P2,O2] = P9(a2); xhi2 = f_xhi(B,F,S2,P2,O2);
    disp(['u1 xhi - : ',num2str(xhi2)])

    % Generate xhi with small parameter difference +
    a3(z) = a3(z)+step4;
    [S3,P3,O3] = P9(a3); xhi3 = f_xhi(B,F,S3,P3,O3);
    disp(['u1 xhi + : ',num2str(xhi3)])

    if xhi2 < xhi1
        S = S2; P = P2; O = O2;
        diff = xhi1-xhi2;
        a3 = a2;
    elseif xhi3 < xhi1
        S = S3; P = P3; O = O3;
        diff = xhi1-xhi3;
        a2 = a3;
    else
        a2(z) = a2(z)+step4;
        a3(z) = a3(z)-step4;
        step4 = step4/10;
        d(4) = d(4)+1; %Update amount of digits of parameter
    end
    %Generate xhi with correct decreasing parameters
    xhi1 = f_xhi(B,F,S,P,O);

%Parameter u2
elseif z == 5 && d(5) <= D
    % Generate xhi with small parameter difference -
    a2(z) = a2(z)-step5;
    [S2,P2,O2] = P9(a2); xhi2 = f_xhi(B,F,S2,P2,O2);
    disp(['u2 xhi - : ',num2str(xhi2)])

    % Generate xhi with small parameter difference +
    a3(z) = a3(z)+step5;
    [S3,P3,O3] = P9(a3); xhi3 = f_xhi(B,F,S3,P3,O3);
    disp(['u2 xhi + : ',num2str(xhi3)])

    if xhi2 < xhi1
        S = S2; P = P2; O = O2;
        diff = xhi1-xhi2;
        a3 = a2;
    elseif xhi3 < xhi1
        S = S3; P = P3; O = O3;
        diff = xhi1-xhi3;
        a2 = a3;
    else

```

```

        a2(z) = a2(z)+step5;
        a3(z) = a3(z)-step5;
        step5 = step5/10;
        d(5) = d(5)+1; %Update amount of digits of parameter
    end
    %Generate xhi with correct decreasing parameters
    xhi1 = f_xhi(B,F,S,P,0);

%Parameter u3
elseif z == 6 && d(6) <= D
    % Generate xhi with small parameter difference -
    a2(z) = a2(z)-step6;
    [S2,P2,O2] = P9(a2); xhi2 = f_xhi(B,F,S2,P2,O2);
    disp(['u3 xhi - : ',num2str(xhi2)])

    % Generate xhi with small parameter difference +
    a3(z) = a3(z)+step6;
    [S3,P3,O3] = P9(a3); xhi3 = f_xhi(B,F,S3,P3,O3);
    disp(['u3 xhi + : ',num2str(xhi3)])

    if xhi2 < xhi1
        S = S2; P = P2; O = O2;
        diff = xhi1-xhi2;
        a3 = a2;
    elseif xhi3 < xhi1
        S = S3; P = P3; O = O3;
        diff = xhi1-xhi3;
        a2 = a3;
    else
        a2(z) = a2(z)+step6;
        a3(z) = a3(z)-step6;
        step6 = step6/10;
        d(6) = d(6)+1; %Update amount of digits of parameter
    end
    %Generate xhi with correct decreasing parameters
    xhi1 = f_xhi(B,F,S,P,0);

%Parameter o1
elseif z == 7 && d(7) <= D
    % Generate xhi with small parameter difference -
    a2(z) = a2(z)-step7;
    [S2,P2,O2] = P9(a2); xhi2 = f_xhi(B,F,S2,P2,O2);
    disp(['o1 xhi - : ',num2str(xhi2)])

    % Generate xhi with small parameter difference +
    a3(z) = a3(z)+step7;
    [S3,P3,O3] = P9(a3); xhi3 = f_xhi(B,F,S3,P3,O3);
    disp(['o1 xhi + : ',num2str(xhi3)])

    if xhi2 < xhi1
        S = S2; P = P2; O = O2;
        diff = xhi1-xhi2;
        a3 = a2;
    elseif xhi3 < xhi1
        S = S3; P = P3; O = O3;

```

```

        diff = xhi1-xhi3;
        a2 = a3;
    else
        a2(z) = a2(z)+step7;
        a3(z) = a3(z)-step7;
        step7 = step7/10;
        d(7) = d(7)+1; %Update amount of digits of parameter
    end
    %Generate xhi with correct decreasing parameters
    xhi1 = f_xhi(B,F,S,P,O);

%Parameter o2
elseif z == 8 && d(8) <= D
    % Generate xhi with small parameter difference -
    a2(z) = a2(z)-step8;
    [S2,P2,O2] = P9(a2); xhi2 = f_xhi(B,F,S2,P2,O2);
    disp(['o2 xhi - : ',num2str(xhi2)])

    % Generate xhi with small parameter difference +
    a3(z) = a3(z)+step8;
    [S3,P3,O3] = P9(a3); xhi3 = f_xhi(B,F,S3,P3,O3);
    disp(['o2 xhi + : ',num2str(xhi3)])

    if xhi2 < xhi1
        S = S2; P = P2; O = O2;
        diff = xhi1-xhi2;
        a3 = a2;
    elseif xhi3 < xhi1
        S = S3; P = P3; O = O3;
        diff = xhi1-xhi3;
        a2 = a3;
    else
        a2(z) = a2(z)+step8;
        a3(z) = a3(z)-step8;
        step8 = step8/10;
        d(8) = d(8)+1; %Update amount of digits of parameter
    end
    %Generate xhi with correct decreasing parameters
    xhi1 = f_xhi(B,F,S,P,O);

%Parameter o3
elseif z == 9 && d(9) <= D
    % Generate xhi with small parameter difference -
    a2(z) = a2(z)-step9;
    [S2,P2,O2] = P9(a2); xhi2 = f_xhi(B,F,S2,P2,O2);
    disp(['o3 xhi - : ',num2str(xhi2)])

    % Generate xhi with small parameter difference +
    a3(z) = a3(z)+step9;
    [S3,P3,O3] = P9(a3); xhi3 = f_xhi(B,F,S3,P3,O3);
    disp(['o3 xhi + : ',num2str(xhi3)])

    if xhi2 < xhi1
        S = S2; P = P2; O = O2;
        diff = xhi1-xhi2;

```

```

        a3 = a2;
elseif xhi3 < xhi1
    S = S3; P = P3; O = O3;
    diff = xhi1-xhi3;
    a2 = a3;
else
    a2(z) = a2(z)+step9;
    a3(z) = a3(z)-step9;
    step9 = step9/10;
    d(9) = d(9)+1; %Update amount of digits of parameter
end
%Generate xhi with correct decreasing parameters
xhi1 = f_xhi(B,F,S,P,O);

end %end of if loop for parameter execution

if (d(1)==D+1) && (d(2)==D+1) && (d(3)==D+1) && (d(4)==D+1) &&...
    (d(5)==D+1) &&(d(6)==D+1) && (d(7)==D+1) && (d(8)==D+1) &&...
    (d(9)==D+1)
    D = D + 1; %loop to increase the digit equally in all parameters
end
v_xhi(z,1)=xhi1;
disp([num2str('xhi retained: '),num2str(xhi1),...
    num2str(' loop N°: '),num2str(1)])

end % end of secondary loop (1:9)

M_9p{1,1} = S; M_9p{2,1} = P; M_9p{3,1} = O;

end % end of main loop

% At the end, save the parameters in a text-file
writematrix(a2,'parameters_for_calibration');

```

9.2 Matlab function to calculate the misfit

```

% Function to calculate misfit xhi

function [xhi] = f_xhi(B,F,S,P,O)
    sigma_b = 1;
    B_temp = zeros(3,length(F));

    for i = 1:length(F)
        B_temp(:,i) = inv(P)*inv(S)*(F(:,i)-O);
    end

    B_scalar = sqrt(B_temp(1,:).^2 + B_temp(2,:).^2 + B_temp(3,:).^2);
    xhi = sum((-B_scalar + B ./ sigma_b).^2);
end

```

9.3 Matlab function to generate the matrices and the vector

```
% Function to generate matrices (sensitivity, angle) and vector (offset)

function [S,P,O] = P9(A)
pj = 3.14159265359;

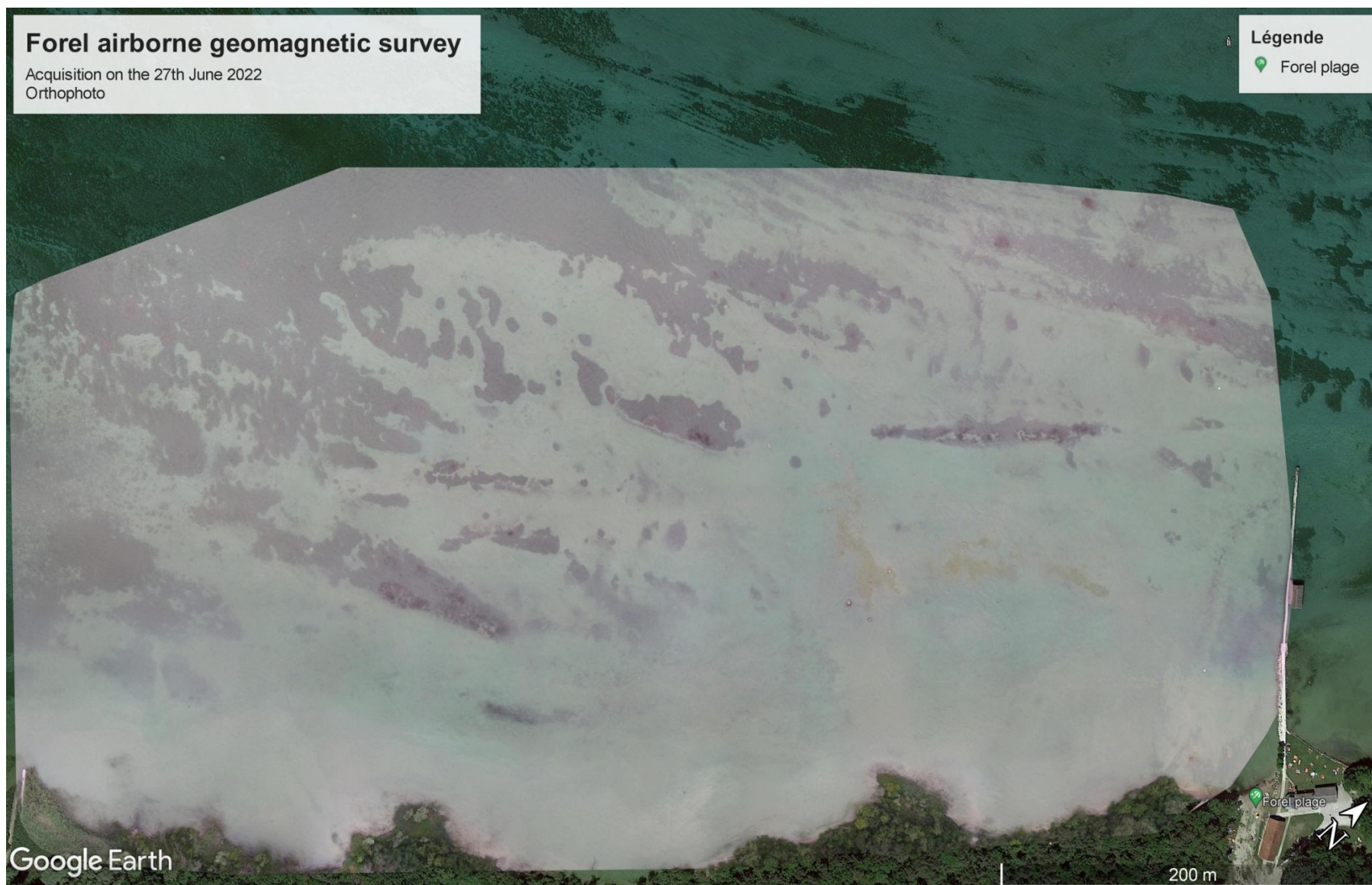
s1 = A(1);
s2 = A(2);
s3 = A(3);
u1 = A(4)*pj/180;
u2 = A(5)*pj/180;
u3 = A(6)*pj/180;
o1 = A(7);
o2 = A(8);
o3 = A(9);

S = [s1 0 0;...
     0 s2 0;...
     0 0 s3];

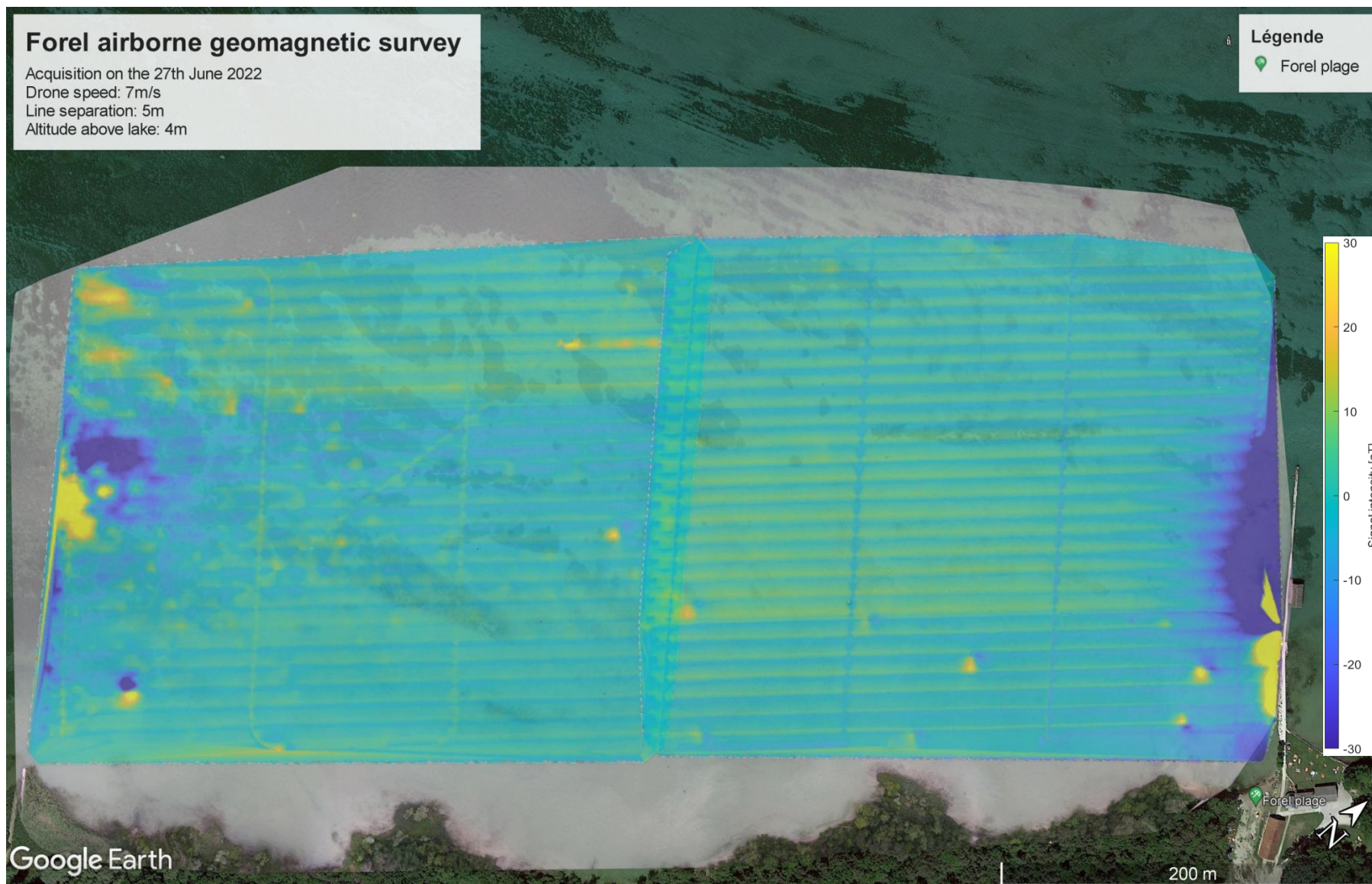
P = [1 0 0;...
     -sin(u1) cos(u1) 0;...
     sin(u2) sin(u3) sqrt(1-(sin(u2)^2)-(sin(u3)^2))];

O = [o1;...
     o2;...
     o3];
end
```

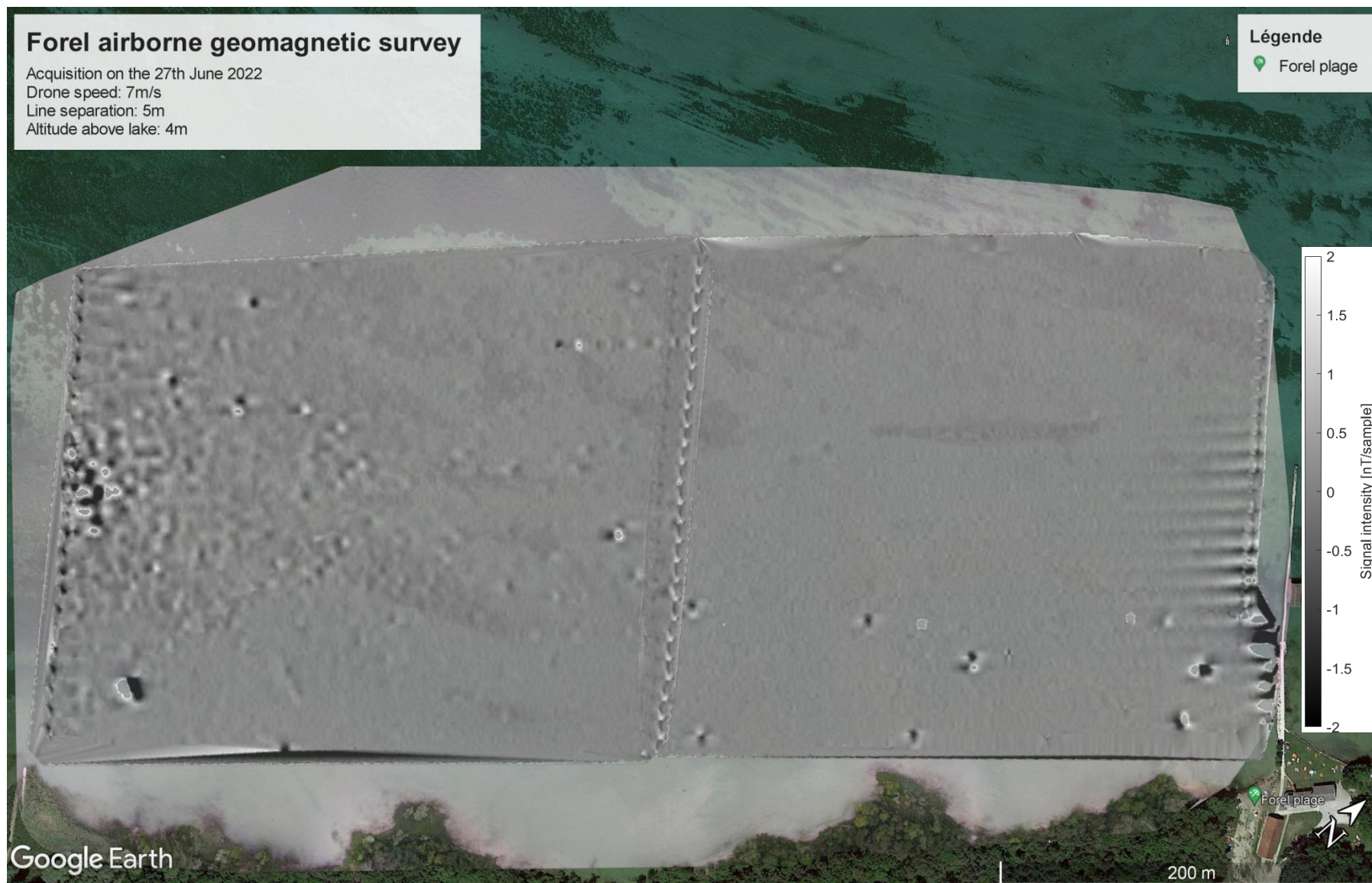
9.4 Forel orthophoto (June 2022)



9.5 Forel magnetic map (June 2022)



9.6 Forel gradient map (June 2022)



9.7 Declaration of originality



Eidgenössische Technische Hochschule Zürich
Swiss Federal Institute of Technology Zurich

Declaration of originality

The signed declaration of originality is a component of every semester paper, Bachelor's thesis, Master's thesis and any other degree paper undertaken during the course of studies, including the respective electronic versions.

Lecturers may also require a declaration of originality for other written papers compiled for their courses.

I hereby confirm that I am the sole author of the written work here enclosed and that I have compiled it in my own words. Parts excepted are corrections of form and content by the supervisor.

Title of work (in block letters):

AIRBORNE GEOMAGNETIC MAPPING WITH AN UNMANNED AERIAL VEHICLE:
DEVELOPMENT OF A SENSOR CALIBRATION SCHEME

Authored by (in block letters):

For papers written by groups the names of all authors are required.

Name(s):

AUBERT

First name(s):

FRANCO

With my signature I confirm that

- I have committed none of the forms of plagiarism described in the ['Citation etiquette'](#) information sheet.
- I have documented all methods, data and processes truthfully.
- I have not manipulated any data.
- I have mentioned all persons who were significant facilitators of the work.

I am aware that the work may be screened electronically for plagiarism.

Place, date

29.07.2022

Signature(s)

For papers written by groups the names of all authors are required. Their signatures collectively guarantee the entire content of the written paper.

10. Funding and acknowledgements

This research was performed with the support of the geothermal energy and geofluids group from the institute of geophysics at the Earth Science Department of the ETH Zürich.

Very special thanks to Friedemann Samrock for his kindness and support in stressful times as well as his personal engagement in this project.